

Multiwavelength mock galaxy catalogues of the low-redshift Universe

Aseem Paranjape¹★, Tirthankar Roy Choudhury²★ and Ravi K. Sheth^{3,4}★

¹Inter-University Centre for Astronomy & Astrophysics, Ganeshkhind, Post Bag 4, Pune 411007, India

²National Centre for Radio Astrophysics, TIFR, Post Bag 3, Ganeshkhind, Pune 411007, India

³Center for Particle Cosmology, University of Pennsylvania, 209 S. 33rd St., Philadelphia, PA 19104, USA

⁴The Abdus Salam International Center for Theoretical Physics, Strada Costiera, 11, Trieste I-34151, Italy

Accepted 2021 March 8. Received 2021 February 24; in original form 2021 January 8

ABSTRACT

We present a new suite of mock galaxy catalogues mimicking the low-redshift Universe, based on an updated halo occupation distribution (HOD) model and a scaling relation between optical properties and the neutral hydrogen (H I) content of galaxies. Our algorithm is constrained by observations of the luminosity function and luminosity- and colour-dependent clustering of *Sloan Digital Sky Survey* (SDSS) galaxies, as well as the H I mass function and H I-dependent clustering of massive H I-selected galaxies in the Arecibo Legacy Fast ALFA (ALFALFA) survey. Mock central and satellite galaxies with realistic values of *r*-band luminosity, $g - r$ and $u - r$ colour, stellar mass and H I mass are populated in an *N*-body simulation, inheriting a number of properties of the density and tidal environment of their host haloes. The host halo of each central galaxy is also ‘baryonified’ with realistic spatial distributions of stars as well as hot and cold gas, along with the corresponding rotation curve. Our default HOD assumes that galaxy properties are a function of group halo mass alone, and can optionally include effects such as galactic conformity and colour-dependent galaxy assembly bias. The mocks predict the relation between the stellar mass and H I mass of massive H I galaxies, as well as the 2-point cross-correlation function of spatially co-located optical and H I-selected samples. They enable novel null tests for galaxy assembly bias, provide predictions for the H I velocity width function, and clarify the origin and universality of the radial acceleration relation in the Lambda cold dark matter framework.

Key words: galaxies: formation – cosmology: theory – dark matter – large-scale structure of Universe – methods: numerical.

1 INTRODUCTION

Contemporary studies of galaxy evolution and cosmology must explore a multitude of physical and statistical properties of the observed large-scale structure of the Universe. The computational and technical challenges involved in any such analysis, whether observational or theoretical, mean that mock galaxy catalogues are now a staple tool of cosmological analyses.

Current and upcoming large-volume surveys of the Universe, aiming to extract cosmological information using observables including the redshift space clustering of galaxies at large and small scales, weak lensing, the abundances of clusters and voids, etc., increasingly rely on the use of mock galaxy catalogues for a variety of applications. Apart from calibrating expected measurement covariances and end-to-end pipeline testing (Mao et al. 2018), such catalogues also serve as excellent test-beds for exploring ideas related to the galaxy–dark matter connection, the nature of dark matter or the predictions of alternative gravity theories, and the effects of dark energy. As such, it is critical to develop and calibrate mock-making algorithms, constrained by existing observations, that can accurately account for the multiscale, multiprobe connection between baryonic matter in and around galaxies and the dark cosmic web in which these galaxies reside. This is the primary motivation behind this work.

Computationally speaking, the most efficient algorithms are those which model the baryon–dark matter connection using empirical, statistical tools that are motivated by the Halo model (see Cooray & Sheth 2002, for a review). These include the halo occupation distribution (HOD; Zehavi et al. 2011), conditional luminosity function (CLF; Yang et al. 2018, and references therein) or subhalo abundance matching (SHAM; Behroozi et al. 2019, and references therein) prescriptions that are constrained by observed galaxy abundances and clustering. At the other end of the spectrum, lie full-fledged cosmological hydrodynamical simulations of galaxy formation (e.g. Dubois et al. 2014; Vogelsberger et al. 2014; Schaye et al. 2015; Springel et al. 2018), arguably the most realistic and most expensive tool in computational cosmology. Semi-analytical models (SAMs), which evolve simplified physical descriptions of galaxy formation and evolution within the cosmic web of gravity-only simulations, lie somewhere between full simulations and empirical models, in terms of both computational complexity as well as fidelity to observational constraints (for a recent review, see Somerville & Davé 2015). The present work focuses on HOD models.

Mock-making algorithms based on the HOD or SHAM frameworks have been frequently used in the literature in conjunction with large-volume surveys at low and intermediate redshifts (de la Torre & Peacock 2013; de la Torre et al. 2013; Manera et al. 2013; Kitaura et al. 2016; Mao et al. 2018; Alam et al. 2020; Sugiyama et al. 2020; Zhao et al. 2020). These algorithms typically segregate into those describing stellar populations and overall star formation activity (constrained by a multitude of galaxy surveys at low- and

* E-mail: aseem@iucaa.in (AP); tirth@ncra.tifr.res.in (TRC); shethrk@physics.upenn.edu (RKS)

high-redshift spanning wavelengths from the infrared to optical to ultraviolet), and others focused on the distribution of gas, primarily in the form of neutral hydrogen (H I, constrained by radio wavelength observations, typically at low redshift). We broadly refer to the former category using the label ‘optical’ and the latter as ‘H I’ algorithms. All such algorithms typically rely on dark haloes identified in gravity-only cosmological simulations, along with statistical prescriptions to paint galaxies into these haloes.

Algorithms for assigning single band optical luminosities (or stellar masses) to mock galaxies using HOD, CLF, or SHAM prescriptions have existed for about two decades (Cooray & Sheth 2002; Vale & Ostriker 2004; Reddick et al. 2013), with relatively recent extensions to include colours (or star formation rates) (Skibba & Sheth 2009; Hearin & Watson 2013; Contreras, Angulo & Zennaro 2020). While the simplest occupation models single out halo mass as the primary driver of observed correlations between galaxy properties and their environments (e.g. Abbas & Sheth 2007; Zu & Mandelbaum 2015; Paranjape, Hahn & Sheth 2018b; Alam et al. 2019), recent work has argued for the importance of modelling beyond-mass effects such as assembly bias and galactic conformity (Zentner, Hearin & van den Bosch 2014), leading to tune-able prescriptions for these effects (Masaki, Lin & Yoshida 2013; Paranjape et al. 2015; Hearin et al. 2016a; Yuan, Eisenstein & Garrison 2018; Contreras et al. 2020; Xu, Zehavi & Contreras 2020). State-of-the-art implementations such as the UNIVERSEMACHINE prescription of Behroozi et al. (2019) employ SHAM on entire merger trees in high-resolution gravity-only simulations, calibrated to reproduce stellar mass functions and star formation rates over a wide range of redshifts.

On the H I side, mock catalogues have been created using a combination of galaxy formation SAMs and a prescription for distributing the H I in discs (see e.g. Obreschkow et al. 2009), which have been useful for planning upcoming surveys with telescopes such as the Square Kilometre Array (SKA). If one is only interested in the very large scale correlations of the H I distribution (e.g. for intensity mapping experiments), or in interpreting H I detections based on stacking experiments at high redshift, the algorithms for creating the catalogues are considerably simpler, assigning an H I mass directly to dark haloes using a physically motivated prescription (Bagla, Khandai & Datta 2010; Guha Sarkar et al. 2012; Villaescusa-Navarro et al. 2014; Castorina & Villaescusa-Navarro 2017; Padmanabhan, Refregier & Amara 2017).

In this paper, we aim to combine low-redshift ($z \lesssim 0.1$) constraints on galaxy abundances and clustering, from surveys of both optically selected as well as H I-selected galaxies, to generate mock galaxies that are simultaneously assigned multiband optical information as well as H I masses. To this end, we consolidate recent work in these areas and introduce mock galaxy catalogues constructed using updated halo occupation models and calibration of multiwavelength low-redshift galaxy optical and H I properties. Each mock galaxy in our catalogues is assigned values of the r -band absolute magnitude M_r (detailed definition below), colour indices $g - r$ and $u - r$, H I mass $m_{\text{H I}}$ and stellar mass m_* , along with a range of environmental properties derived from the dark matter environment of the galaxy’s host halo. Relying on these properties, the mocks reproduce the luminosity function and the luminosity and colour dependence of projected 2-point clustering of *Sloan Digital Sky Survey* (SDSS) galaxies, the H I mass function and $m_{\text{H I}}$ -dependent clustering of massive ALFALFA galaxies, and predict the cross-correlations between these galaxies. The mocks also have tunable implementations of galactic conformity (Weinmann et al. 2006) and colour-dependent galaxy assembly bias (Hearin & Watson 2013; Paranjape et al. 2015).

Additionally, the host halo of each central galaxy in our mocks is ‘baryonified’, i.e. assigned a realistic spatial distribution of stars and gas and, consequently, a realistic rotation curve for the galactic disc. This is a novel feature of our mocks which, as we discuss later, potentially allows us to explore a number of interesting questions that have not been adequately addressed in the theoretical literature. Among others, these include modelling the observed 21-cm line profiles of H I-selected galaxies, along with the associated velocity width distribution, and the nature and universality of the radial acceleration relation in the baryons + cold dark matter (CDM) paradigm.

The rest of the paper is organized as follows. We describe the ingredients of our mock algorithm in Section 2, followed by a detailed description of the algorithm itself in Section 3. In Section 4, we demonstrate the performance of our mocks in reproducing a number of 1-point and 2-point statistical observables. In Section 5, we discuss observables whose behaviour is *predicted* by our mocks, along with possible extensions of our technique that are interesting for future analyses. We conclude in Section 6 with a brief discussion of potential applications of our mocks.

Throughout, we consider a flat Λ CDM cosmology with parameters $\{\Omega_m, \Omega_b, h, n_s, \sigma_8\}$ given by $\{0.276, 0.045, 0.7, 0.961, 0.811\}$ compatible with the 7-yr results of the *Wilkinson Microwave Anisotropy Probe* experiment (WMAP7; Komatsu et al. 2011), with a linear theory transfer function generated by the code CAMB (Lewis, Challinor & Lasenby 2000).¹ Our convention will be to quote halo masses (m) in $h^{-1}M_\odot$ and galaxy stellar masses (m_*) and H I masses ($m_{\text{H I}}$) in $h^{-2}M_\odot$ units. The notation m for halo mass will refer to m_{200b} , the mass enclosed in the radius R_{200b} , where the enclosed density falls to 200 times the background density. Similarly m_{vir} will refer to m_{200c} , the mass enclosed in the radius R_{200c} , where the enclosed density falls to 200 times the critical density.

2 INGREDIENTS

We start by describing the ingredients used in constructing our mocks. These include the gravity-only simulations that we populate with galaxies, the observed galaxy sample whose optical properties form the basis of the HOD, we use to assign luminosities, colours, and stellar masses to the mock galaxies, and the scaling relation between optical properties and neutral hydrogen (H I) using which we assign H I masses.

2.1 Simulations

The N -body simulations, we rely on are listed in table 1 of Paranjape & Alam (2020), of which we focus on the WMAP7 configurations. Specifically, we have 2, 10, and 3 realizations each of the L150_N1024, L300_N1024, and L600_N1024 boxes, respectively, corresponding to particle masses $m_p = 2.41 \times 10^8, 1.93 \times 10^9, 1.54 \times 10^{10} h^{-1} M_\odot$, respectively. The notation L150_N1024, for example, indicates a cubic, periodic box of length $L_{\text{box}} = 150 h^{-1} \text{Mpc}$ containing 1024^3 particles. The simulations were performed using the tree-PM code GADGET-2 (Springel 2005)² with a PM grid of a factor 2 finer than the initial particle count along each axis, and a comoving force softening length of $1/30$ of the mean interparticle spacing. Initial conditions were generated using second-order Lagrangian perturbation theory (Scoccimarro 1998) with the code

¹<http://camb.info>

²<http://www.mpa-garching.mpg.de/gadget/>

MUSIC (Hahn & Abel 2011).³ Haloes were identified using the code ROCKSTAR (Behroozi, Wechsler & Wu 2013a)⁴ which performs a Friends-of-Friends (FoF) algorithm in 6D phase space. We discard all sub-haloes and further only consider objects whose ‘virial’ energy ratio $\eta = 2T/|U|$ satisfies $0.5 \leq \eta \leq 1.5$ (Bett et al. 2007). All the simulations and analysis were performed on the Perseus and Pegasus clusters at IUCAA.⁵

2.2 Galaxy sample

We rely on optical properties of galaxies in the local Universe as provided by Data Release 7 (DR7; Abazajian et al. 2009) of the SDSS (York et al. 2000).⁶ From the SDSS DR7 Catalogue Archive Server (CAS),⁷ we obtained galaxy properties including Galactic extinction-corrected apparent magnitudes (luptitudes) in the u , g , and r bands for all galaxies with spectroscopic redshifts in the range $0.02 \leq z \leq 0.2$ and satisfying the Petrosian r band apparent magnitude threshold $m_r \leq 17.7$. Both Petrosian and Model magnitudes were obtained from the data base. Absolute magnitudes $M_{0.1u}$, $M_{0.1g}$, $M_{0.1r}$ were estimated by K-correcting to rest-frame bands at $z = 0.1$ using K-CORRECT (Blanton & Roweis 2007) (we used a modified version of the PYTHON wrapper provided by N. Raseliasarison⁸) and evolution correcting as described by Blanton et al. (2003). We did not correct for dust extinction in the host, which makes edge-on spirals appear redder. This makes our colour-dependent analysis consistent with that of Zehavi et al. (2011) who reported measurements of colour-dependent clustering using similarly uncorrected colours. Correcting for inclination can, in principle, affect inferences regarding the physics of quenching in satellites, as well as the physics governing the H I content of optically red galaxies, which we will explore in future work. [Consistency with Zehavi et al. (2011) is also why we do not work with the improved SDSS photometry discussed in Meert, Vikram & Bernardi (2015).] Flux measurement errors were accounted for when using K-CORRECT, but not explicitly in the Gaussian mixture fitting below.

This analysis yielded values of $M_r \equiv M_{0.1r} - 5 \log_{10}(h)$, and similarly M_g and M_u , for each galaxy. The latter were converted to the colour indices $g - r = M_g - M_r$ and $u - r = M_u - M_r$, which are therefore rest-frame colours, K-corrected and evolution corrected to $z = 0.1$. Below, we use Petrosian absolute magnitudes M_r and Model colours $g - r$ and $u - r$.

2.3 Optical halo occupation distribution

Here, we discuss the complete optical HOD we use for assigning luminosities and colours to mock galaxies. This HOD is constrained by measurements of luminosity- and colour-dependent clustering in SDSS DR7 and uses a Gaussian mixture description of bi-variate colour distributions, as described below.

2.3.1 Constraints from luminosity-dependent clustering

We use the standard 5-parameter mass-only HOD calibrated by Paul, Pahwa & Paranjape (2019) for the WMAP7 cosmology, which de-

scribes SDSS luminosity-dependent clustering measurements from Zehavi et al. (2011). The HOD was calibrated using simulation-based tables of 2-point halo correlation functions and halo profiles from the $z = 0$ outputs of the simulations described above, following the technique of Zheng & Guo (2016). Satellites were assumed to be distributed according to the spherically averaged dark matter distribution in parent haloes, without assuming the (Navarro, Frenk & White 1996; NFW) profile (although the latter is an excellent approximation over the spatial and mass dynamic range of interest; this will be useful below). For the 2-halo terms, hard-sphere halo exclusion was implemented, but all other correlations were directly measured from the simulations in narrow mass bins, so that non-linear, scale-dependent halo bias was accurately modelled. See Paul et al. (2019) for further discussion.

2.3.2 Constraints from colour dependent clustering

Paul et al. (2019) also modelled colour-dependent clustering from Zehavi et al. (2011) by treating the ‘red fraction’ $f_{r|s}(M_r)$ of satellites of luminosity M_r as a free parameter. Here, $f_{r|s}(M_r)$ is the fraction of satellites in a luminosity bin (labelled M_r) whose $g - r$ colours satisfy

$$g - r > (g - r)_{\text{cut}}(M_r) \equiv 0.21 - 0.03M_r, \quad (1)$$

(equation 13 of Zehavi et al. 2011). Paul et al. (2019) propagated this cut into the halo model formalism to observationally constrain $f_{r|s}(M_r)$ in the four wide luminosity bins for which clustering measurements and jack-knife covariance matrices were available (see their table 1).

The final product provided by Paul et al. (2019) comprises simple fitting functions for the M_r -dependence of the five parameters defining the thresholded HOD and the parameter $f_{r|s}$ in the range $-23 < M_r \leq -19$ (see their figs 12 and 13 and table 3; they denote $f_{r|s}$ as $p_{r|s}$). We use these below to assign luminosities and colours to mock central and satellite galaxies.

2.3.3 Colour distribution

In the following, we require the joint distribution $p(u - r, g - r | M_r)$ of $g - r$ and $u - r$ at fixed M_r in SDSS, which we model as a 2-component bivariate Gaussian mixture. In principle, one can logically extend this analysis to multiple bands using a higher dimensional Gaussian mixture. Likewise, we could use more components in the mixture, but have found that 2 are sufficient for this purpose. We use measured values of $g - r$ and $u - r$ in narrow bins of M_r without accounting for measurement errors. For each bin of M_r , we construct a volume-limited subsample by choosing galaxies in the redshift range $0.02 \leq z < z_{\text{max}}(M_{r,\text{max}})$, where $M_{r,\text{max}}$ is the faint edge of the bin and $z_{\text{max}}(M_{r,\text{max}})$ is the redshift at which a galaxy of this absolute magnitude would fall below the flux limit $m_r = 17.7$ of the survey. We use the PYTHON package `sklearn.mixture` (Pedregosa et al. 2011)⁹ to implement an iterative Expectation-Maximization algorithm (Dempster, Laird & Rubin 1977) with 12 initializations. We repeat the exercise in each luminosity bin for 150 bootstrap resamplings of the respective subsample and use the average values of the 11 parameters defining the Gaussian mixture as the ‘best fit’, with the corresponding standard deviations across the bootstrap samples as errors.

Fig. 1 compares the measured bivariate distributions in a few bins of M_r (coloured histograms) with the best-fitting Gaussian mixture

³<https://www-n.oca.eu/ohahn/MUSIC/>

⁴<https://bitbucket.org/gfcstanford/rockstar>

⁵<http://hpc.iucaa.in>

⁶www.sdss.org

⁷www.skyserver.sdss.org

⁸<https://github.com/nirina/kcorrect.python>

⁹<https://scikit-learn.org/>

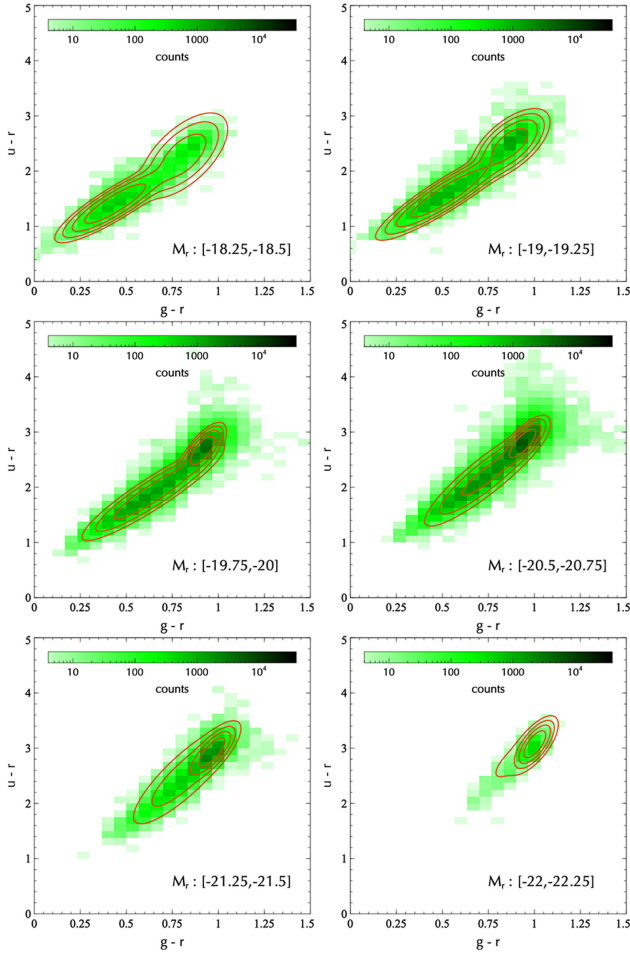


Figure 1. Bivariate distribution of Model $(g-r, u-r)$ colours in bins of Petrosian absolute magnitude M_r (coloured histograms) measured in *SDSS*, compared with the best-fitting Gaussian mixture in each bin (contours).

(contours). Fig. 2 summarizes the 11 parameters of the mixture for all the luminosity bins (points with errors). The parameters are: (i) the probability $p(\text{red}|M_r)$ that the galaxy belongs to the ‘red’ mode of the mixture, (ii) the mean vectors $(\langle g-r|M_r \rangle_{\text{red}}, \langle u-r|M_r \rangle_{\text{red}})$ and $(\langle g-r|M_r \rangle_{\text{blue}}, \langle u-r|M_r \rangle_{\text{blue}})$ of the red and blue modes, respectively, (iii) the diagonal elements of the covariance matrices $(\sigma_{\text{red}}^2(g-r|M_r), \sigma_{\text{red}}^2(u-r|M_r))$ and $(\sigma_{\text{blue}}^2(g-r|M_r), \sigma_{\text{blue}}^2(u-r|M_r))$ of the red and blue modes, respectively, and (iv) the correlation coefficients between $g-r$ and $u-r$, for the red and blue modes, respectively. The smooth curves in Fig. 2 show piecewise continuous polynomial fits to each parameter. These are used similarly to the HOD fitting functions provided by Paul et al. (2019), to assign colours to mock galaxies (see below).

For assigning colours to centrals and satellites separately, we require the probability $p(\text{red}|\text{sat}, M_r)$ that the $g-r$ and $u-r$ colours of a satellite of luminosity M_r are drawn from the ‘red mode’ of the bivariate double-Gaussian distribution described above. This can be easily obtained by combining the constraints on f_{rls} described in Section 2.3.2 with (a subset of) the parameters of the Gaussian mixture $p(g-r, u-r|M_r)$, and is given by

$$p(\text{red}|\text{sat}, M_r) = \frac{2f_{\text{rls}} - \mathcal{I}_{(\text{blue})}(M_r)}{\mathcal{I}_{(\text{red})}(M_r) - \mathcal{I}_{(\text{blue})}(M_r)}, \quad (2)$$

where (suppressing the M_r -dependence of the arguments for brevity)

$$\mathcal{I}_{(\text{red/blue})}(M_r) = \text{erfc} \left(\frac{(g-r)_{\text{cut}} - \langle g-r \rangle_{\text{red/blue}}}{\sqrt{2}\sigma_{\text{red/blue}}(g-r)} \right), \quad (3)$$

and where $(g-r)_{\text{cut}}(M_r)$ was given in equation (1).

2.3.4 Stellar masses

Stellar masses are calculated using a mass-to-light ratio calibrated to *SDSS* DR7 measurements similarly to Paranjape et al. (2015, see their sections 2.3 and 4.2). The measurements are shown as the coloured histogram in Fig. 3. We fit a mean relation to these measurements in bins of $x \equiv (g-r)$, of the form

$$\langle M/L \rangle(x) = a + b \text{erf}((x-c)d) + e \tanh((x-f)/g), \quad (4)$$

finding best-fitting values

$$a = 1.3281; \quad b = 0.735; \quad c = 0.5859, \\ d = 3.38; \quad e = 0.187; \quad f = 0.8976; \quad g = 0.0874. \quad (5)$$

We also fit the scatter around the mean in the same bins, of the form

$$\sigma_{(M/L)}(x) = \begin{cases} k_0 + k_1(x-x_0); & x < x_0 \\ k_0 + k_2(x-x_0) + k_3(x-x_0)^2; & x \geq x_0, \end{cases} \quad (6)$$

finding best-fitting values given by

$$x_0 = 1.019; \quad k_0 = 0.1441; \quad k_1 = -0.182, \\ k_2 = 1.16; \quad k_3 = -0.2. \quad (7)$$

Our calibration is shown in Fig. 3 and is better behaved than that of Paranjape et al. (2015) for very blue objects; we have checked, however, that both calibrations lead to nearly identical results for the final mocks. For each mock galaxy with colour $g-r$, we calculate a Gaussian random number for the mass-to-light ratio with mean and standard deviation calculated using equations (4) and (6), respectively, setting $x = (g-r)$. This is then combined with the corresponding value of M_r of the galaxy to assign a stellar mass m_* .

2.4 Neutral hydrogen masses

Paul, Choudhury & Paranjape (2018, hereafter, PCP18) calibrated a lognormal scaling relation (with constant scatter in log-mass) between the neutral hydrogen mass m_{HI} of a galaxy and its optical properties M_r and $g-r$, using the optical HOD from Guo et al. (2015) and clustering measurements from Guo et al. (2017) of H I-selected galaxies in the Arecibo Legacy Fast ALFA (ALFALFA) survey (Giovanelli et al. 2005). The scaling relation was separately calibrated for central and satellite galaxies using a halo model, along with an overall parameter f_{HI} which gives the fraction of optically selected galaxies that contain H I. Their default model also assumed that satellites with $m_{\text{HI}} > 10^{10.2} \times (0.678/h)^2 M_\odot$ do not exist. The model was constrained using measurements of number counts and projected clustering $w_p(r_p)$ of ALFALFA H I-selected galaxies from Guo et al. (2017) for the thresholds $\log_{10}(m_{\text{HI}}/h^{-2}M_\odot) \geq 9.8 + 2\log_{10}(0.678)$ and $10.2 + 2\log_{10}(0.678)$.

The default PCP18 model precludes rare, massive H I satellites. In the following, we will also see that this default implementation is in mild disagreement with $w_p(r_p)$ for galaxies with $\log_{10}(m_{\text{HI}}/h^{-2}M_\odot) \geq 10.0 + 2\log_{10}(0.678)$ (which was not used in constraining the scaling relation). This is likely due to our updated optical HOD from Paul et al. (2019) with its improved modelling of scale-dependent halo bias and the self-consistent calibration

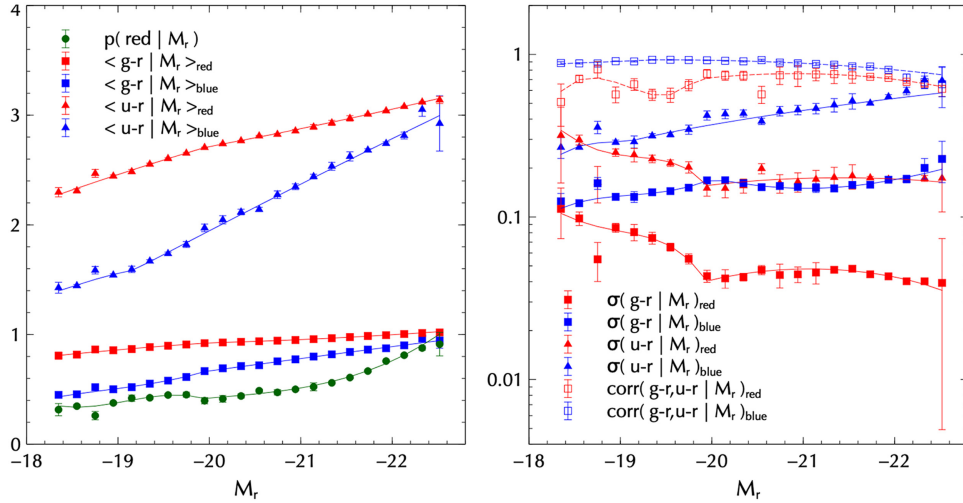


Figure 2. Summary of Gaussian mixture fits for $p(g-r, u-r | M_r)$ (points with errors). Smooth curves show piecewise continuous polynomial fits to each mixture parameter, which we use in assigning colours to mock galaxies.

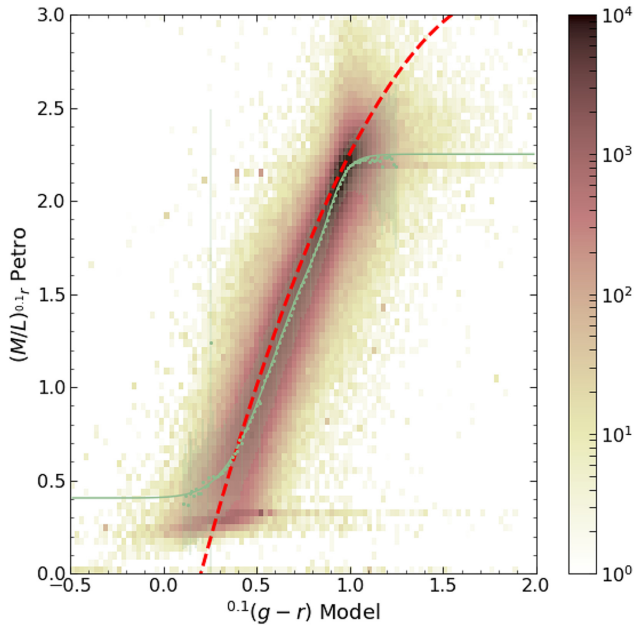


Figure 3. Calibration of mass-to-light ratio for the SDSS DR7 sample, using the code K-CORRECT. Histogram shows the measured distribution of Model $g-r$ colours against Petrosian mass-to-light ratio in the r band. Green points with errors show binned measurements of the same, and the green solid curve shows our best-fitting relation (4) to the points. Dashed red curve shows the fit reported by Wang & White (2012) for reference. See text for discussion.

of the satellite red fraction. (The latter was identified by PCP18 as the parameter most susceptible to systematic effects in their analysis; see their section 4.2.) We therefore explored variations around the PCP18 model, finding that the simple modification of excluding satellites from haloes with $m > m_{\text{sat,max}}$, while keeping the scaling relations for centrals and satellites intact otherwise, leads to acceptable descriptions of the measurements for all the thresholds mentioned above, as well as of the H I mass function. Since the threshold is on halo rather than H I mass, such a model can in principle accommodate rare and massive H I satellites. A simple χ^2 minimization exercise, varying $m_{\text{sat,max}}$ and predicting $w_p(r_p)$ for

galaxies with $\log_{10}(m_{\text{H I}}/h^{-2}M_{\odot}) \geq 10.0 + 2 \log_{10}(0.678)$ using the covariance matrix kindly provided by Hong Guo, leads to $m_{\text{sat,max}} \simeq 10^{14.4} h^{-1} M_{\odot}$.

Being tied to the optical HOD, this H I scaling relation suffers from a natural incompleteness in producing H I masses, determined by the optical completeness limit on M_r for the galaxy population. For a sample limited by $M_r < -19$, for example, the H I mass function is complete only above $m_{\text{H I}} \gtrsim 10^{9.65} h^{-2} M_{\odot}$. As such, all our analysis of H I-selected galaxies is restricted to the massive end.

3 ASSIGNING GALAXY PROPERTIES IN MOCKS

We now describe our main algorithm for generating mock galaxies in a gravity-only simulation, along with a ‘baryonification’ scheme for assigning spatial distributions of stars and gas to each galaxy.

3.1 Algorithm

Our basic algorithm to assign galaxy luminosities and colours to haloes in N -body simulations is essentially the same as that described by Skibba & Sheth (2009), with a few technical improvements. We also include a number of additional galaxy properties. The algorithm can be summarized as follows:

(i) **Central occupation and luminosity:** A threshold luminosity L_{min} (or absolute magnitude $M_{r,\text{max}}$) is dynamically determined by requiring that the HOD of central galaxies $f_{\text{cen}}(> L_{\text{min}} | m)$ be sampled down to a value 1.5×10^{-3} for all halo masses $m \geq 40 m_{\text{part}}$, where m_{part} is the particle mass of the simulation. For example, for the L300_N1024 configuration, this gives us $M_{r,\text{max}} \simeq -19$. Haloes of mass m are then occupied by a central galaxy with probability $f_{\text{cen}}(> L_{\text{min}} | m)$. Central galaxy luminosities are sampled from the conditional luminosity function $f_{\text{cen}}(> L | m) / f_{\text{cen}}(> L_{\text{min}} | m)$.

(ii) **Satellite occupation and luminosity:** The number of satellites in an occupied halo is drawn from a Poisson distribution with mean $\bar{N}_{\text{sat}}(> L_{\text{min}} | m)$, and the luminosities of these satellites are sampled from the conditional luminosity function $\bar{N}_{\text{sat}}(> L | m) / \bar{N}_{\text{sat}}(> L_{\text{min}} | m)$. We do not enforce that satellites be less luminous than their host central. For a luminosity-complete sample of galaxies with $M_r \leq -19$, we find that, in approximately 6.5 per cent of groups

containing at least one satellite, the brightest satellite is brighter than the central.

(iii) **Galaxy positions:** The central of a halo is placed at the halo centre of mass. Satellite positions are distributed as an NFW profile around the central, truncated at R_{200b} . Halo concentrations c_{200b} are drawn from a lognormal distribution with median and scatter at fixed halo mass as calibrated by Diemer & Kravtsov (2015) using very high resolution simulations, which avoids contamination due to numerical fitting errors in relatively low-resolution boxes. The use of the NFW form, which is an accurate description of the profile of well-resolved haloes at the masses and spatial separations of our interest (see e.g. figs 2 and 3 of Paul et al. 2019), also allows us to bypass the need for accessing particle information from the underlying N -body simulation and work only with halo catalogues. The fitting functions from Diemer & Kravtsov (2015, who used the m_{200c} definition of halo mass) are converted to the m_{200b} definition appropriate for the HOD fits using the prescription of Hu & Kravtsov (2003).

To preserve correlations between halo concentration and large-scale environment, the lognormal concentrations of haloes in narrow mass bins are rank ordered by the actual estimated halo concentrations in each bin (the assumption being that this ranking would be approximately preserved even in relatively coarsely sampled haloes, although see Ramakrishnan, Paranjape & Sheth 2020). The scale radius $r_s = R_{200b}/c_{200b}$ inferred for each halo from this exercise is stored for later use (see Section 3.2).

(iv) **Galaxy velocities:** The central of a halo is assigned the bulk velocity of the halo. The satellites are assigned random velocities drawn from a 3D isotropic Gaussian distribution with mean equal to the central velocity and 1-d velocity dispersion appropriate for the NFW profile at the location of the satellite.

Additionally, we implement the following modifications:

(i) **Galaxy colours:** To assign $g-r$ and $u-r$ colours to galaxies, we extend the algorithm proposed by Skibba & Sheth (2009). As in their case, the first step is to determine whether a galaxy is ‘red’ or ‘blue’, which is done separately for satellites and centrals, using the probability $p(\text{red}|\text{sat}, M_r)$ for satellites (see Section 2.3.3) and the corresponding probability for centrals which can be derived using $p(\text{red}|\text{sat}, M_r)$, $p(\text{red}|M_r)$, and the HOD (this also requires an integral over the halo mass function, for which we use the fitting function from Tinker et al. 2008). In the next step, we assign $g-r$ and $u-r$ colours by sampling the appropriate (bivariate) mode of the double Gaussian $p(g-r, u-r|M_r)$ calibrated in Section 2.3.3. Operationally, we first sample the univariate mode $p_{\text{red/blue}}(g-r|M_r)$ (obtained by marginalizing the respective bivariate distribution over $u-r$) and then sample the corresponding conditional distribution $p_{\text{red/blue}}(u-r|g-r, M_r)$, for each red/blue galaxy (see also Xu et al. 2018). Optionally, we also include galactic conformity by correlating $g-r$ with halo concentration (or an unspecified Gaussian-distributed halo property) at fixed halo mass, using the tunable prescription of Paranjape et al. (2015).

(ii) **Galaxy stellar masses:** As discussed by Paranjape et al. (2015) and described in detail in Section 2.3.4, we calculate stellar masses m_* using a $(g-r)$ -dependent mass-to-light ratio calibrated for SDSS DR7 galaxies.

(iii) **Galaxy neutral hydrogen masses:** We assign HI masses to a uniformly sampled fraction f_{HI} of galaxies, with a lognormal distribution at fixed M_r and $g-r$, using the model from PCP18. This model, which we refer to as the ‘minimal PCP18’ model below, additionally discards HI-satellites which have $\log_{10}(m_{\text{HI}}/h^{-2}M_\odot) > 10.2 + 2\log_{10}(0.678)$. As described in Section 2.4, we modify this model by instead discarding HI-satellites in parent haloes having

$m \geq m_{\text{sat,max}}^{10}$. This is done *after* the uniform downsampling for HI assignment described above. For our default model, which we call ‘PCP18 mod-sat’, we set $m_{\text{sat,max}} = 10^{14.4} h^{-1} M_\odot$ (see below for a comparison between the models). As discussed by PCP18, for optically selected galaxies with $M_r \leq -18$, this optical–HI scaling relation places the majority of HI mass in faint blue galaxies (see their Fig. 9).

(iv) **Neutral hydrogen discs:** For each galaxy containing HI, we assign a comoving disc scale length h_{HI} for an assumed thin disc with HI surface density $\Sigma_{\text{HI}}(r_\perp) \propto e^{-r_\perp/h_{\text{HI}}}$ (here r_\perp is the radial distance in the disc plane), using the scaling relation

$$h_{\text{HI}} = 7.49 h^{-1} \text{kpc} (m_{\text{HI}}/10^{10} h^{-2} M_\odot)^{0.5}, \quad (8)$$

with a scatter of 0.06 dex, consistent with the measurements reported by Wang et al. (2016).¹¹ These are useful in modelling ‘baryonified’ rotation curves, as we describe later.

(v) **Galaxy environment:** We assign to each galaxy the value of its host-centric dark matter overdensity δ and tidal anisotropy α , each Gaussian smoothed at an adaptive scale $4R_{200b,\text{host}}/\sqrt{5}$ and at the fixed scale $2h^{-1} \text{Mpc}$, as well as the bias b_1 of the host (see Paranjape, Hahn & Sheth 2018a and Paranjape & Alam 2020 for how these variables are calculated in the N -body simulation).

3.2 ‘Baryonified’ density profiles and rotation curves

The galaxy properties described above, namely, luminosity, colour, stellar mass, and HI mass, are all assigned by our algorithm by treating each galaxy as a point object. Combined with the information on the host halo mass and concentration; however, these properties can also be used to model the *spatial distribution* of stars and of hot and cold gas in the galaxy and its halo. This in turn can be used to construct a rotation curve for the galaxy, which has several interesting applications as we discuss later.

Since the circular velocity $v_{\text{rot}}(r)$ at a halocentric distance r depends on the total mass $m_{\text{tot}}(< r)$ enclosed in this radius, we must model the spatial distribution of *all* matter components inside the host halo. This is particularly relevant for the inner parts of the halo which are typically baryon dominated. We restrict this analysis to central galaxies and will return in future work to satellite galaxies, which require additional modelling of processes such as tidal and ram pressure stripping, strangulation, etc. (see e.g. van den Bosch et al. 2008; Behroozi et al. 2019) that are beyond the scope of this work.

We follow the prescription of Schneider & Teyssier (2015, henceforth, ST15) to ‘baryonify’ each host halo. This method, and extensions thereof, have been shown to successfully account for baryonic effects in the matter power spectrum (Chisari et al. 2018; Schneider et al. 2019; Aricò et al. 2020b) and bispectrum (Aricò et al. 2020a) at relatively small scales over a range of redshifts. We have modified the ST15 prescription to include the HI disc and have simplified it by truncating all profiles at the halo radius (see e.g. Aricò et al. 2020b). Following the general practice for this method, we use the mass $m_{\text{vir}} \equiv m_{200c}$ and radius $R_{\text{vir}} \equiv R_{200c}$ for all baryonification scaling relations below. We are primarily interested

¹⁰All such ‘discarded’ satellites continue to have their assigned optical properties, only their HI mass is set to zero.

¹¹Wang et al. (2016) provide a scaling relation for the quantity D_{HI} defined as the diameter of the contour corresponding to a surface density of $1 M_\odot \text{pc}^{-2}$, which we relate to h_{HI} using the provided scaling relation itself (which implies a constant average surface density, independent of m_{HI}) along with an integral over the exponential disc profile $\Sigma_{\text{HI}}(r_\perp)$.

here in low redshifts and length-scales $\lesssim R_{\text{vir}}$. We briefly summarize the method next.

(i) Before baryonification, each halo starts with its total matter as a single component distributed according to an NFW profile consistent with the gravity-only simulation in which the mock catalogue is being generated, using the mass m_{vir} and concentration $c_{\text{vir}} = R_{\text{vir}}/r_s$ (see Section 3.1 for details of determining the scale radius r_s for each halo).

(ii) We divide the total mass of each baryonified halo into 5 components: bound gas ('bgas'), stars in the central galaxy ('cgal'), neutral hydrogen in its disc ('HI'),¹² gas expelled due to feedback ('egas'), and the dark matter which quasi-adiabatically relaxes in the presence of the baryons ('rdm').

(iii) Each baryonic component, denoted by index $\alpha \in \{\text{bgas}, \text{cgal}, \text{HI}, \text{egas}\}$, is assigned a mass fraction f_α subject to the constraint $f_{\text{bary}} \equiv \sum_\alpha f_\alpha = \Omega_b/\Omega_m$ due to conservation of baryonic mass. In practice, we set $f_{\text{cgal}} = m_*/m_{\text{vir}}$, $f_{\text{HI}} = 1.33 m_{\text{HI}}/m_{\text{vir}}$ (with the pre-factor accounting for helium correction), and f_{bgas} using

$$f_{\text{bgas}} = (\Omega_b/\Omega_m) \times [1 + (M_c/m_{\text{vir}})^\beta]^{-1}, \quad (9)$$

with $M_c = 1.2 \times 10^{14} h^{-1} M_\odot$ and $\beta = 0.6$ as described by ST15 (see their equation 2.19 and Fig. 2). We comment on possible variations in this relation later. The ejected gas fraction f_{egas} is then set by the baryonic mass conservation constraint.¹³

(iv) Each baryonic component is given its own mass profile $\rho_\alpha(r)$. The choices below for ρ_{bgas} , ρ_{cgal} , and ρ_{egas} are identical to those in ST15. We briefly describe these below and refer the reader to ST15 for more details and original references.

(a) The bound gas component refers to the hot, ionized halo gas (which does not include, e.g. gas heated by supernovae). The corresponding density profile ρ_{bgas} has the form $\rho_{\text{bgas}} \propto [\ln(1 + r/r_s)/(r/r_s)]^{1/(\Gamma-1)}$, set assuming hydrostatic equilibrium and a polytropic equation of state in the inner halo and matched to the original NFW profile in the outer halo. Here, r_s and Γ are the scale radius of the NFW profile and the polytropic index of the gas, respectively. The matching is performed at a radius $r_{\text{match}} = \sqrt{5} r_s$ and fixes the value of Γ . For hosts of centrals with $M_r \leq -19$, we find typical values of $\Gamma \simeq 1.19$ with a dispersion of $\simeq 0.015$.

(b) The stellar profile is assumed to follow $\rho_{\text{cgal}} \propto r^{-2} e^{-r^2/4R_{\text{hl}}^2}$ with half-light radius $R_{\text{hl}} = 0.015 R_{\text{vir}}$ (Kravtsov 2013). In principle, this can be extended to include a scatter and/or accommodate a dependence on halo angular momentum as predicted by disc formation models (Mo, Mao & White 1998, see the discussion in Kravtsov 2013); we ignore this here for simplicity. Strictly speaking, we should treat the stellar profile as a combination of a central bulge and a 2D disc (with a relative contribution that correlates with galaxy colour), rather than the purely spherically symmetric form assumed here. In this work, we will follow the previous literature on the subject and assume

the form given above, leaving a more self-consistent description of the stellar disc to future work. In this sense, the stellar profile we model is better thought of as a pure bulge.

(c) The expelled gas component incorporates all gas affected by feedback, without distinguishing between possible gas phases. Its profile is taken to be $\rho_{\text{egas}}(r) \propto e^{-r^2/2r_{\text{ej}}^2}$ with $r_{\text{ej}} = 0.5\sqrt{200} \eta_{\text{ej}} R_{\text{vir}}$, setting $\eta_{\text{ej}} = 0.5$, so that $r_{\text{ej}} \simeq 3.5 R_{\text{vir}}$. As discussed by ST15, the modelling of $\rho_{\text{egas}}(r)$ in the halo outskirts is rather uncertain and observationally ill-constrained. However, at the scales of our interest ($r \lesssim R_{\text{vir}}$), $\rho_{\text{egas}}(r) \approx$ constant, and its contribution to the total mass is therefore completely determined by baryonic mass conservation inside the halo. Our results are therefore expected to be very robust to any minor variations in the shape of $\rho_{\text{egas}}(r)$ at scales $\gtrsim R_{\text{vir}}$.

(d) The sphericalized profile of HI is obtained by integrating a thin exponential disc of surface density $\Sigma_{\text{HI}}(r_\perp) \propto e^{-r_\perp/h_{\text{HI}}}$ (with r_\perp being the radial distance in the disc plane) to get $\rho_{\text{HI}}(r) \propto r^{-1} e^{-r/h_{\text{HI}}}$. The disc scale length h_{HI} is assigned as described in Section 3.1. **Note:** This sphericalized contribution only affects the calculation of the relaxed dark matter component. The contribution of the HI disc to the rotation curve itself is treated separately as described below.

Each profile function $\rho_\alpha(r)$ is normalized so as to enclose the total mass m_{vir} inside R_{vir} . The total baryonic profile is then $f_{\text{bary}} \rho_{\text{bary}}(r) = \sum_\alpha f_\alpha \rho_\alpha(r)$, with an enclosed baryonic mass $m_{\text{bary}}(<r) = 4\pi \int_0^r dr' r'^2 f_{\text{bary}} \rho_{\text{bary}}(r')$.

(v) The dark matter component is assumed to quasi-adiabatically respond to the presence of baryonic mass and relax to a new shape while approximately conserving angular momentum. The details of the iterative procedure used to calculate the resulting relaxed dark matter profile $\rho_{\text{rdm}}(r)$ (normalized similarly to the baryonic profile functions) are in Appendix A, which is based on section 2.3 of ST15. The mass fraction f_{rdm} is set simply by mass conservation to be $f_{\text{rdm}} = 1 - \Omega_b/\Omega_m$. The dark matter mass enclosed in radius r is then $m_{\text{rdm}}(<r) = 4\pi \int_0^r dr' r'^2 f_{\text{rdm}} \rho_{\text{rdm}}(r')$.

(vi) The thin exponential HI disc leads to a mid-plane circular velocity contribution $v_{\text{HI}}(r)$ satisfying (see section 2.6 of Binney & Tremaine 1987)

$$v_{\text{HI}}^2(r) = \frac{2f_{\text{HI}}V_{\text{vir}}^2}{(h_{\text{HI}}/R_{\text{vir}})} y^2 [I_0(y)K_0(y) - I_1(y)K_1(y)], \quad (10)$$

where $y \equiv r/(2h_{\text{HI}})$, $V_{\text{vir}} = \sqrt{Gm_{\text{vir}}/R_{\text{vir}}}$ is the virial velocity and $I_n(y)$ and $K_n(y)$ are modified Bessel functions of the first and second kind, respectively.

(vii) The total mass of dark matter and all baryonic components except the HI disc enclosed in radius r is $m_{\text{tot-HI}}(<r) = m_{\text{rdm}}(<r) + m_{\text{bary-HI}}(<r)$, where the notation 'bary-HI' refers to summing over all baryonic components except HI. Since we truncate all profiles at the radius R_{vir} of the host halo, the total halo mass satisfies $m_{\text{vir}} = m_{\text{tot-HI}}(<R_{\text{vir}}) + 1.33 m_{\text{HI}}$. Finally, the rotational velocity $v_{\text{rot}}(r)$ of a test particle at halocentric distance r in the galaxy mid-plane is

$$v_{\text{rot}}(r) = \sqrt{Gm_{\text{tot-HI}}(<r)/r + v_{\text{HI}}^2(r)}. \quad (11)$$

Fig. 4 shows baryonified density profiles and rotation curves for hypothetical dwarf-like and Milky Way-like haloes hosting an NGC 99-like galaxy, comparing the baryonified result with the original NFW result in each case. Only for these examples, we have set the galaxy stellar mass using the abundance matching prescription of Behroozi, Wechsler & Conroy (2013b) with updated parameters taken from Kravtsov, Vikhlinin & Meshcheryakov (2018), and have

¹²We assume that the stellar and HI discs are decoupled and do not model time-dependent warps, etc. in the HI disc. We correct for helium as mentioned in the text but do not attempt to account for molecular hydrogen.

¹³For a small fraction (~ 1 per cent) of objects with $M_r \leq -19$, the sum $f_{\text{cgal}} + f_{\text{HI}} + f_{\text{bgas}}$ exceeds Ω_b/Ω_m (these in turn are dominated by objects having $f_{\text{cgal}} + f_{\text{HI}} > \Omega_b/\Omega_m$). For such objects, we set $f_{\text{egas}} = 0$ without changing any of the other baryonic mass fractions, so that $f_{\text{bary}} > \Omega_b/\Omega_m$. Overall mass conservation then implies that the corresponding dark matter fraction $f_{\text{rdm}} = 1 - f_{\text{bary}}$ is smaller than $1 - \Omega_b/\Omega_m$ for these objects.

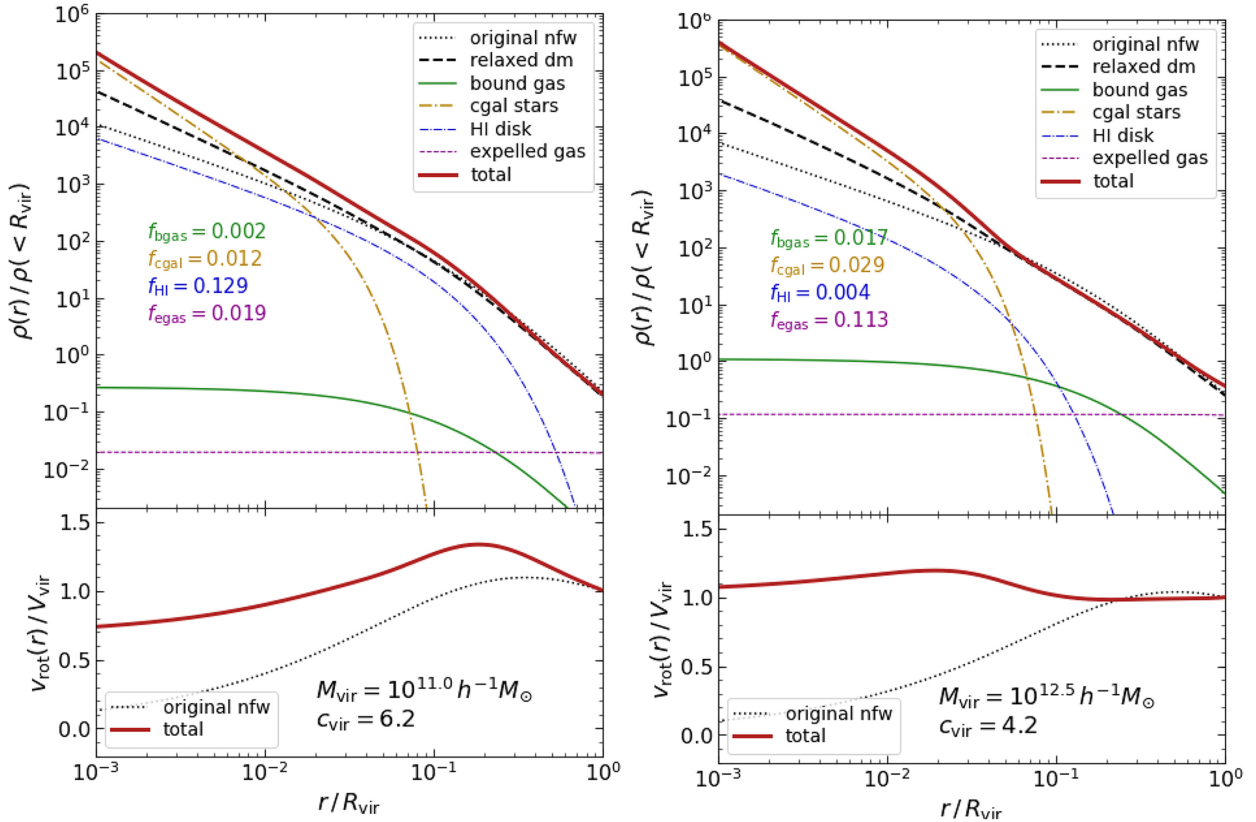


Figure 4. Baryonification of haloes from gravity-only simulations. We show two examples of hypothetical haloes with masses $m_{\text{vir}} = 10^{11} h^{-1} M_{\odot}$ (left-hand panels) and $m_{\text{vir}} = 10^{12.5} h^{-1} M_{\odot}$ (right-hand panels), with halo concentrations and baryonic mass fractions as indicated in respective labels. The baryonic fractions sum up to $\Omega_b/\Omega_m \simeq 0.163$. *Upper panels:* Density profiles normalized by the halo density $\rho(< R_{\text{vir}}) \equiv 200\rho_{\text{crit}}$. The original NFW profile in each case is shown by the thin dotted black curve. Thicker curves with different colours and line styles show the 5 individual components as indicated, with the thick dark red curve showing the final total profile. Note especially that the ejected gas profile (dotted magenta) is nearly a constant in each case, and that the relaxed dark matter profile (thick dashed black) is substantially different from the original NFW in its shape due to quasi-adiabatic contraction and expansion. *Lower panels:* Rotation velocity profile $v_{\text{rot}}(r)$ normalized by the virial velocity $V_{\text{vir}} = \sqrt{Gm_{\text{vir}}/R_{\text{vir}}}$. Note that the contribution of the H I disc to the rotation curve is treated separately from that of the spherical components, as described in the text.

fixed the H I mass to $m_{\text{H I}} = 10^{9.83} h^{-2} M_{\odot}$, with the H I disc size set using equation (8).

We clearly see that the ejected gas profile is essentially constant in each case. More importantly, we see that the baryonified rotation curves are substantially flatter and also more diverse in shape than their purely NFW counterparts (see also Section 5.1).

4 RESULTS

We now report the results of generating mock catalogues using the algorithm of Section 3 on the simulations described in Section 2.1.

4.1 Optical properties

As a sanity check, the *left-hand panel* of Fig. 5 compares the input fitting functions for the HOD from Paul et al. (2019) with the output of the mock algorithm applied to a single L300.N1024 box. The *right-hand panel* of the figure compares the thresholded luminosity function averaged over 6 realizations of the L300.N1024 box with the measurements from Zehavi et al. (2011) that were used as constraints by Paul et al. (2019).

Fig. 6 similarly compares the projected clustering of red/blue/all galaxies in mock catalogues with the measurements from Zehavi

et al. (2011). Mock galaxies were classified as red and blue based on their $g - r$ values in comparison to equation (1) to ensure a fair comparison with the data. The projected 2-point correlation function (2pcf) $w_p(r_p)$ for mock galaxies was calculated by integrating the real space 2pcf $\xi(r)$ using

$$w_p(r_p) = 2 \int_{r_p}^{\sqrt{r_p^2 + \pi_{\text{max}}^2}} dr \frac{r \xi(r)}{\sqrt{r^2 - r_p^2}}, \quad (12)$$

where we set $\pi_{\text{max}} = 60 h^{-1} \text{Mpc}$ to match the Zehavi et al. (2011) measurements. We see generally good agreement in all cases, although the clustering of red galaxies tends to be lower in the mock than in the data. This is very likely due to the limited volume of our $300 h^{-1} \text{Mpc}$ boxes, which do not include the effects of faint (predominantly red) satellites in very massive haloes.

Fig. 7 shows the joint distributions of M_r , $g - r$, and $u - r$ in one mock using the L300.N1024 box. We clearly see the well-known colour-magnitude and colour-colour bimodality, another sanity check on the mock algorithm.

Turning to somewhat more detailed tests, Fig. 8 compares the differential luminosity and stellar mass functions averaged over 6 realizations of the L300.N1024 box with fitting functions to SDSS measurements from the literature. In each case, for the mock measurements we show results separately for red/blue/all

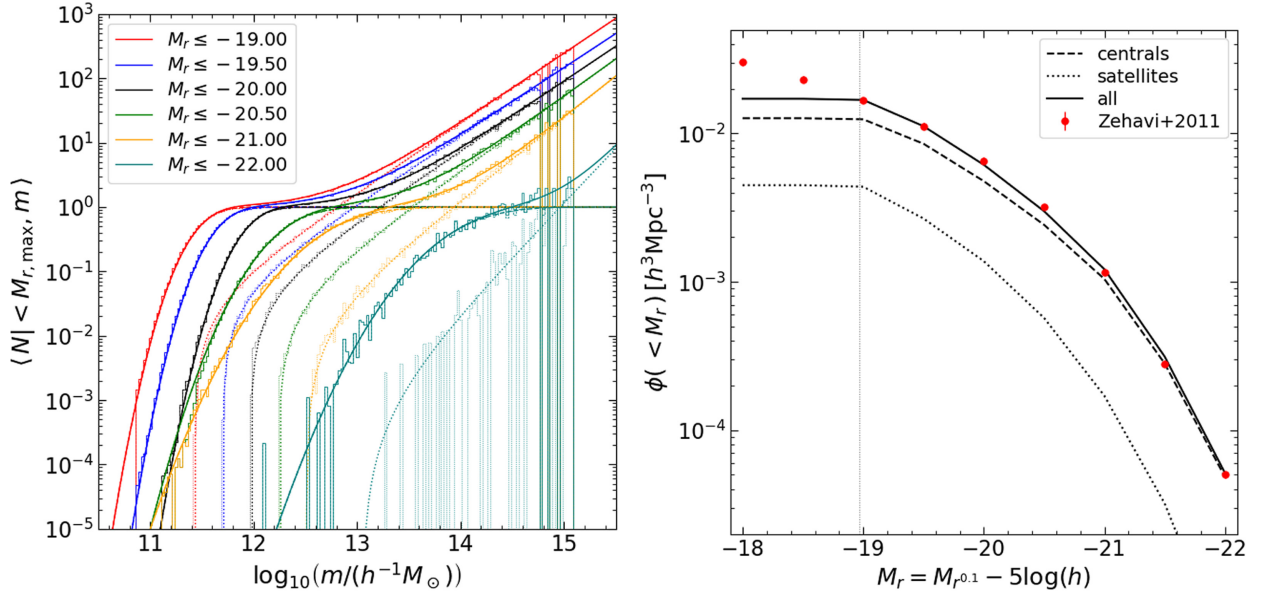


Figure 5. Sanity check on HOD. (*Left-hand panel:*) Mocks versus input functions. For each threshold on M_r , we separately show the contribution of central and satellite galaxies in the mock (histograms) and in the analytical HOD (smooth curves). (*Right-hand panel:*) Thresholded luminosity function in the mock (separately showing the contribution of central, satellite, and all galaxies) versus *SDSS* data from Zehavi et al. (2011). Vertical dotted line indicates the completeness threshold calculated by our algorithm for the L300_N1024 box.

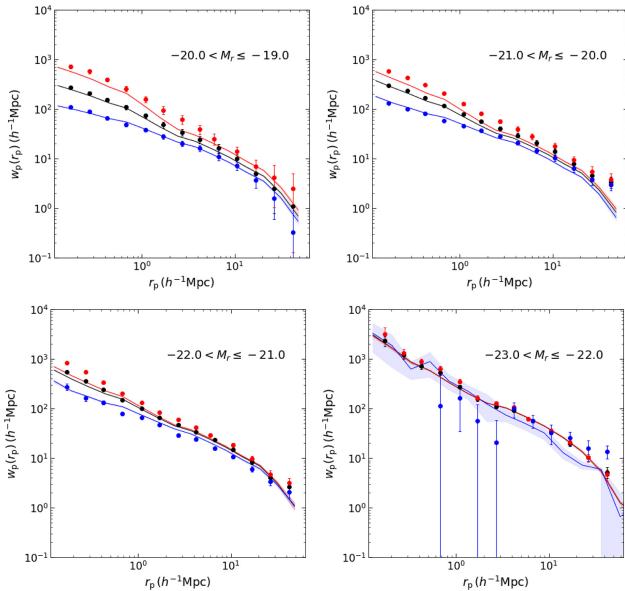


Figure 6. Sanity check on clustering. Projected 2-point correlation function (2pcf) $w_p(r_p)$ for red/blue/all galaxies in luminosity bins in the mock (solid lines with error bands) compared with data from Zehavi et al. (2011, points with errors). Mock measurements used 6 realizations of the L300_N1024 box for the three fainter bins and 3 realizations of the L600_N1024 box for the brightest bin. Lines show the mean and error bands reflect the respective standard deviations over all available realizations. Similarly to the data, mock galaxies were classified as red and blue based on their $g-r$ values in comparison to equation (1). The 2pcf for mock galaxies was calculated using equation (12) with $\pi_{\text{max}} = 60 h^{-1} \text{Mpc}$ to match the Zehavi et al. (2011) measurements.

central/satellite/all galaxies. The total luminosity function is in reasonable agreement with the Schechter function fit from Blanton et al. (2003), which is not very surprising since the thresholded luminosity function was used as a constraint in the HOD calibration. The total

stellar mass function of the mocks also agrees reasonably well with the corresponding fit from Peng et al. (2012). In this case, we also have individual fits for centrals and satellites, which were produced by Peng et al. (2012) using the *SDSS* group catalogue of Yang et al. (2007), which similarly agree well with the stellar mass functions of mock centrals and satellites, respectively. Considering the substantial amount of systematic uncertainty involved in extracting stellar mass functions from data, as well as inherent systematics in the galaxy classification algorithm used to produce the *SDSS* group catalogue, we conclude that the mocks are in good agreement with the data here as well.

4.2 Neutral hydrogen properties

Fig. 9 compares the H I mass function and projected 2pcf in the ‘minimal PCP18’ model (see Section 3.1) with measurements in the ALFALFA survey. The *left-hand panel* shows the differential H I mass function of red/blue/all central/satellite/all galaxies averaged over 6 realizations of the L300_N1024 box, compared with the fit to H I-selected galaxies in the ALFALFA survey by Martin et al. (2010). We see reasonable agreement above the completeness limit of the catalogue (set by the luminosity completeness threshold; see section 2.4 and the discussion in Paul et al. 2018). The *right-hand panel* shows that the 2pcf of mock galaxies with $\log_{10}(m_{\text{H I}}/h^{-2}M_{\odot}) > 10.0 + 2\log_{10}(0.678)$ compares slightly worse with the corresponding ALFALFA measurements from Guo et al. (2017) than the higher $m_{\text{H I}}$ thresholds, which perform well. The 2pcf for H I-selected mock galaxies was calculated using equation (12) with $\pi_{\text{max}} = 20 h^{-1} \text{Mpc}$ to match the Guo et al. (2017) measurements.

As mentioned earlier, this slight disagreement is likely due to our use of an updated and improved optical HOD. We therefore explore the modification of the PCP18 model described in Section 3.1 and discard H I-selected satellites in parent haloes with $m \geq m_{\text{sat,max}}$. To set the value of the threshold, we attempted to minimize the χ^2 between mocks and data for the threshold

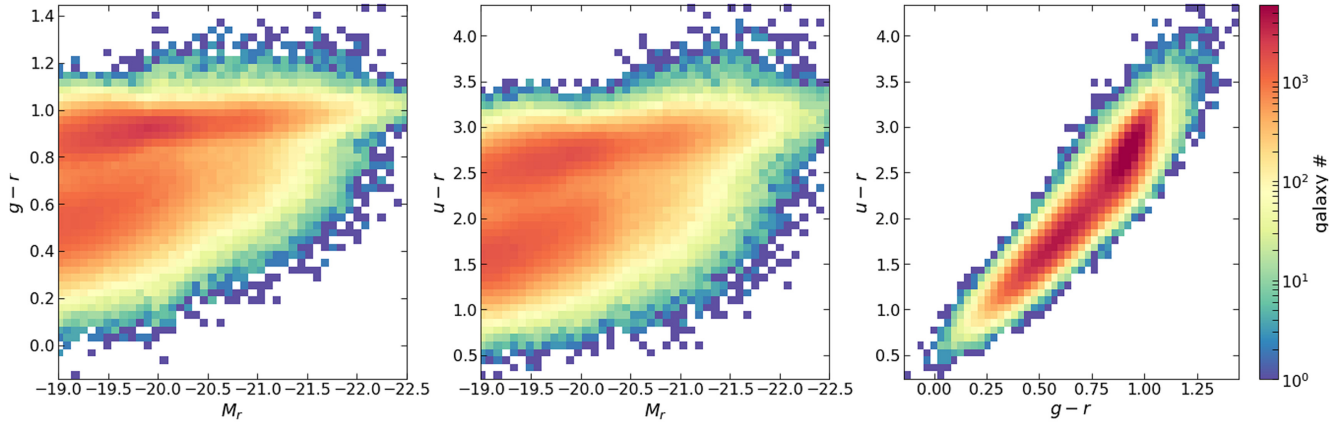


Figure 7. Colour–magnitude and colour–colour bimodality in the mock. Histograms show distributions of M_r against $g - r$ (left-hand panel) and $u - r$ (middle panel), and $g - r$ against $u - r$ (right-hand panel) in one mock using the L300_N1024 box.

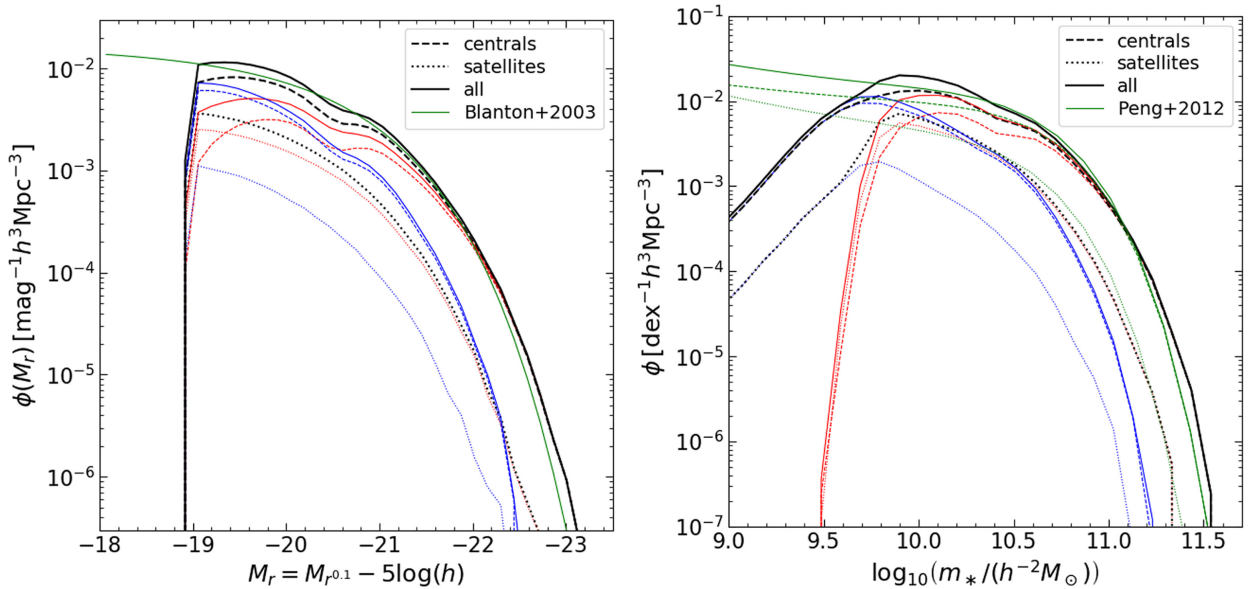


Figure 8. Differential luminosity functions (left-hand panel) and stellar mass functions (right-hand panel) of red/blue/all central/satellite/all galaxies averaged over 6 mocks using the L300_N1024 configuration. Colour segregation in the left-hand panel was based on equation (1) applied to $g - r$ and M_r for each galaxy, while for the right-hand panel we used $(g - r)_{\text{cut}} = 0.76 + 0.10[\log_{10}(m_*/h^{-2} M_{\odot}) - 10]$ (Paranjape et al. 2015). For comparison, the solid green curves in the left-hand (right-hand) panel show the corresponding SDSS fits from Blanton et al. (2003) (Peng et al. 2012). In the case of the stellar mass function, these fits are also separately available for centrals and satellites and are shown as the dashed and dotted green curves, respectively.

$\log_{10}(m_{\text{H I}}/h^{-2} M_{\odot}) \geq 10.0 + 2 \log_{10}(0.678)$. We found that the χ^2 has a very broad minimum in the vicinity of $m_{\text{sat,max}} = 10^{14.4} h^{-1} M_{\odot}$, which we use as our default value. The resulting H I mass function and projected 2pcf are shown in Fig. 10; we see a mild improvement in the 2pcf of the lowest threshold, and also some improvement in the higher thresholds. Since this halo thresholded model, which we refer to as ‘PCP18 mod-sat’, allows for the existence of massive satellites while still agreeing with observations, we choose to adopt it as our default model. For comparison, the number densities in units of $(h^{-1} \text{Mpc})^{-3}$ in this model for each thresholded sample (in order of increasing threshold H I mass) in the mocks are, respectively, $\{2.274 \pm 0.003, 0.810 \pm 0.002, 0.203 \pm 0.0007\} \times 10^{-3}$ (with errors estimated using the scatter across 6 realizations), while the corresponding values from table 1 of Guo et al. (2017) are $\{2.68, 0.92, 0.22\} \times 10^{-3}$ (no errors are provided on these values).

We have also explored several ‘beyond halo mass’ modifications of the PCP18 model by changing the criterion used for discarding H I-selected satellites. In particular, we considered thresholds on (i) halo mass and concentration jointly (i.e. only allowing satellites in low mass and high concentration haloes), (ii) halo concentration alone (only high-concentration haloes allowed), (iii) large-scale linear halo bias (low bias haloes allowed), and (iv) discarding all ‘red mode’ satellites. These are generally inspired by the results of Guo et al. (2017), who found that abundance matching preferentially younger (sub)haloes with H I-selected galaxies led to good descriptions of ALFALFA clustering. Of these, a joint threshold on halo mass and concentration performs the best, but leads to minimum χ^2 values nearly identical to those for the ‘PCP18 mod-sat’ model above, at the cost of one additional parameter. We therefore conclude that the ALFALFA data for massive H I galaxies *do not require* ‘beyond

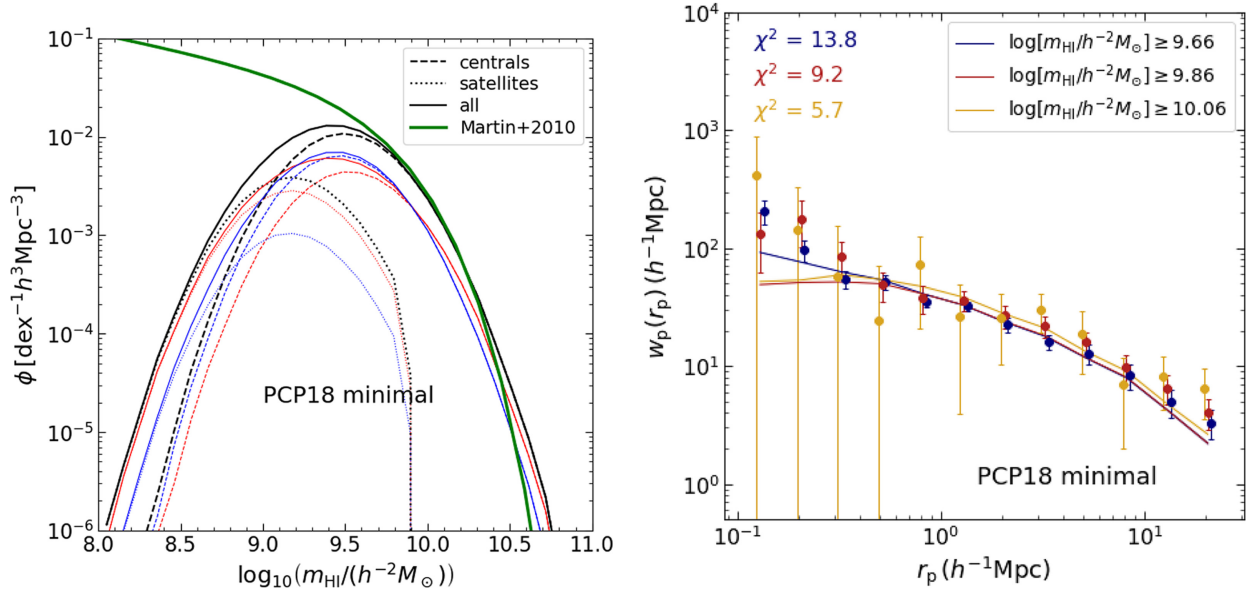


Figure 9. (Left-hand panel): Differential H I mass function of red/blue/all central/satellite/all galaxies in averaged over 6 ‘minimal PCP18’ model mocks using the L300_N1024 configuration. Colour segregation was based on equation (1) applied to $g - r$ and M_r for each galaxy. For comparison, the solid green curves show the corresponding fit from Martin et al. (2010) to H I-selected galaxies in the ALFALFA survey. (Right-hand panel): Projected 2pcf in the ‘minimal PCP18’ model (averaged over the same mocks as in the left-hand panel) for three m_{HI} thresholds, compared with corresponding ALFALFA measurements from Guo et al. (2017). The labels indicate the values of χ^2 when comparing each mock result with the corresponding 12 data points from the ALFALFA measurements using the covariance matrices kindly provided by Hong Guo.

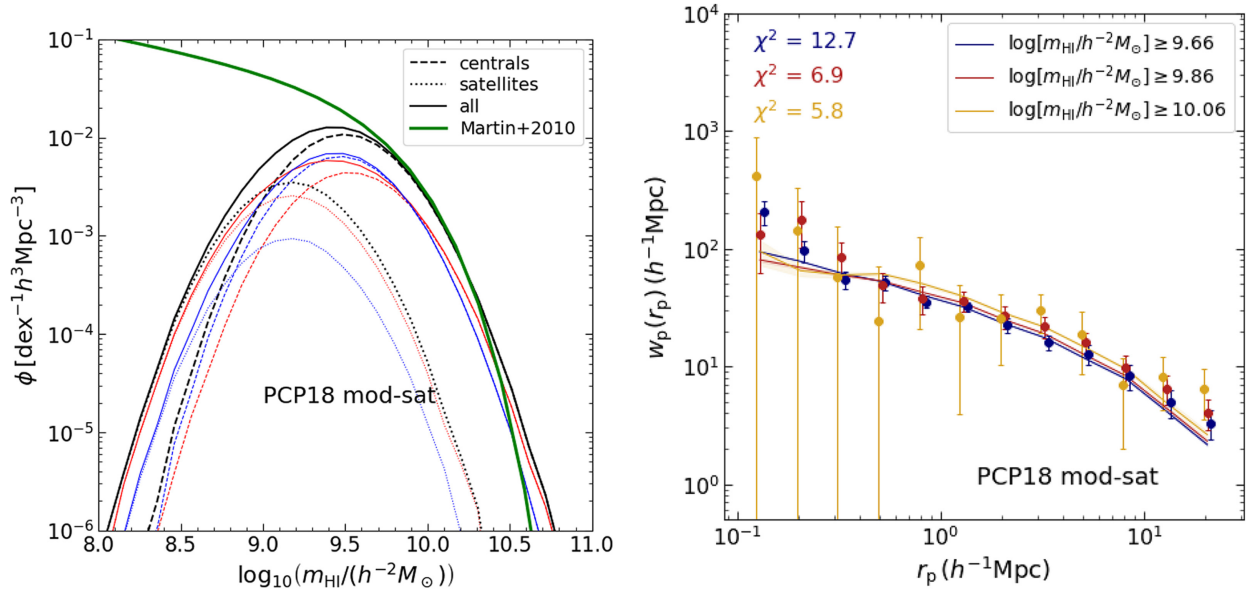


Figure 10. Same as Fig. 9, showing results for the ‘PCP18 mod-sat’ model described in Section 3.1, which discards H I-selected satellites in parent haloes with $m \geq m_{\text{sat,max}}$. The value of $m_{\text{sat,max}}$ was set to $10^{14.4} h^{-1} M_{\odot}$ by minimizing the χ^2 between the mock 2pcf results and corresponding ALFALFA measurements and covariance for the lowest mass threshold shown. We adopt this as our default model for assigning H I mass to mock galaxies.

halo mass’ effects in modelling the mass function and projected 2pcf, provided that H I mass is assigned through an optical scaling relation.

5 PREDICTIONS AND EXTENSIONS

Having demonstrated that our mock catalogues reproduce the basic 1-point and 2-point observables associated with galaxy samples

selected by optical or H I properties, in this section we discuss certain predictions of our mocks, along with a few possible extensions.

5.1 Rotation curves and baryon mass–halo mass relations

Fig. 11 shows the rotation curves of 150 randomly chosen mock central galaxies containing H I discs, with the curves in each panel being coloured by one of m_* , M_r , m_{HI} , or $g - r$. As noted

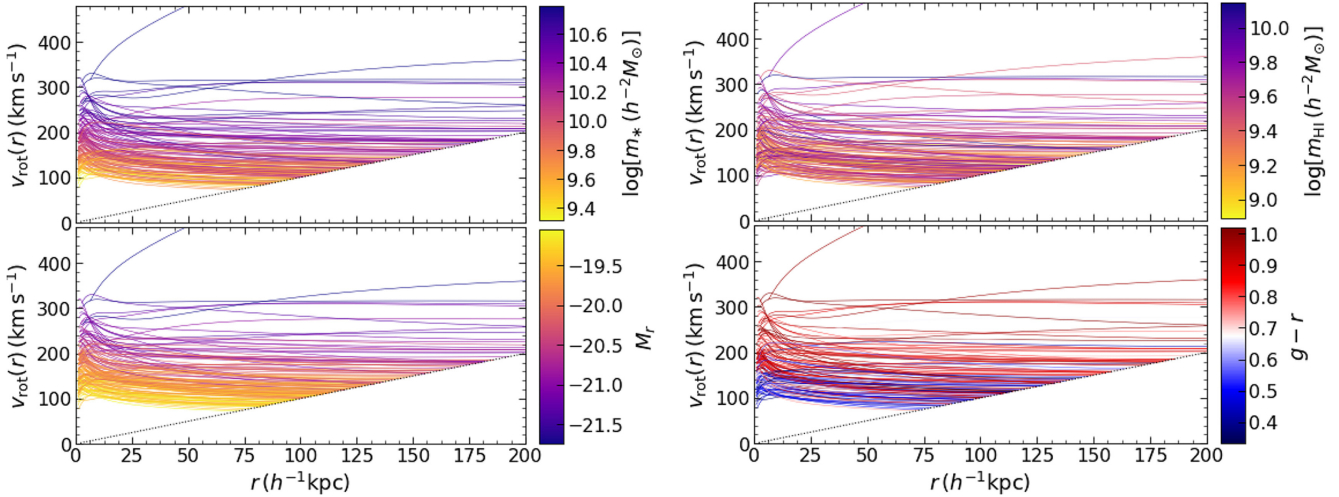


Figure 11. Rotation curves of 150 central galaxies containing H I discs, chosen at random from one mock using the L300.N1024 configuration. Each curve is coloured by the galaxy’s stellar mass m_* (top left), luminosity M_r (bottom left), H I mass m_{HI} (top right), and colour $g - r$ (bottom right). Since each rotation curve is only generated for $r \leq R_{\text{vir}}$, the curves truncate at the dotted line which shows $v(r) = (V_{\text{vir}}/R_{\text{vir}})r$ in each panel.

earlier, these are generally flat but show considerable diversity, in qualitative agreement with observed rotation curves (Persic, Salucci & Stel 1996; McGaugh, Rubin & de Blok 2001). We defer a more quantitative comparison with observations to future work.

Our mocks also predict the relations between group halo mass and stellar mass (m_*-m) as well as H I mass ($m_{\text{HI}}-m$). Fig. 12 shows the m_*-m relation (top panel) and the $m_{\text{HI}}-m$ relation (bottom panel) for all central galaxies with $M_r \leq -19$ in one mock using the L300.N1024 configuration. The top panel is essentially the same as fig. A4 of Paranjape et al. (2015), except that we have used an updated HOD. Similarly, the bottom panel can be compared with fig. B1 of PCP18, who showed the median $m_{\text{HI}}-m$ relation using their analytical halo model. Both sets of results are consistent with these earlier works, showing a steep m_*-m relation but a much shallower $m_{\text{HI}}-m$ relation. The latter feature also emphasizes the need for caution when painting H I directly into haloes: the weak correlation between H I mass and halo mass can amplify systematic errors in any calibration.

For comparison, the purple curves in the top panel show the median m_*-m relations calibrated using SHAM by Behroozi et al. (2013b, solid) and Kravtsov et al. (2018, dash-dotted), converted in each case to the m_{200b} mass definition appropriate for this work. We see that, for stellar masses above the completeness limit of our mocks (horizontal dotted line), the mock result is closer to the Behroozi et al. (2013b) relation for $m \lesssim 10^{13.5} h^{-1} M_\odot$ and lies between the two SHAM calibrations at larger halo masses. A similar comparison with the literature for the $m_{\text{HI}}-m$ relation is complicated by the fact that different authors have used different conventions for defining this relation (e.g. Guo et al. 2017; Padmanabhan et al. 2017). We have checked that our results are qualitatively similar to these calibrations, leaving a more detailed analysis to future work.

5.2 H I-optical cross-correlations

A primary strength of our mock algorithm is its ability to paint realistic optical and H I properties in the same galaxies. This means that we can go beyond previous studies and predict or forecast expectations for the joint distribution of, say, stellar and H I mass in low-redshift galaxies, along with the corresponding spatial correlations.

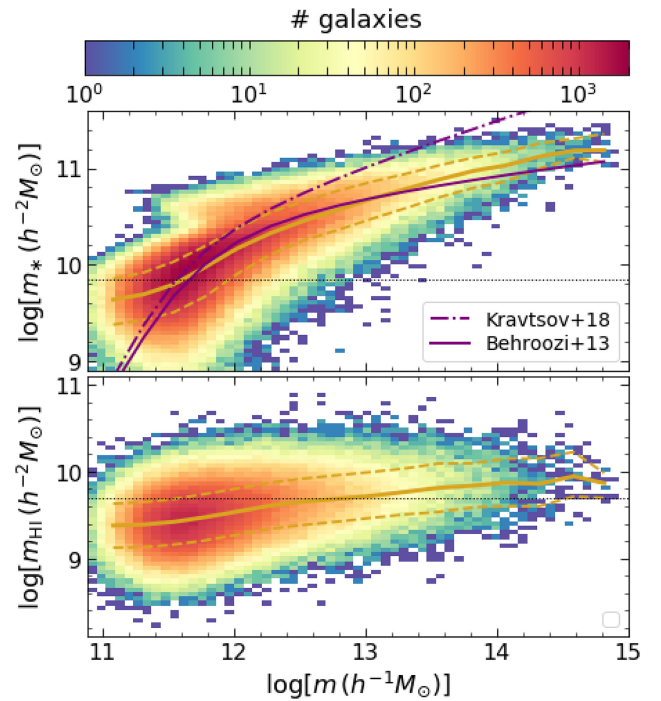


Figure 12. Correlation with halo mass. Histograms show the m_*-m (top panel) and $m_{\text{HI}}-m$ (bottom panel) relation for all central galaxies with $M_r \leq -19$ in one mock using the L300.N1024 configuration. Solid yellow lines in each panel show the median relation in bins of halo mass, while dashed yellow lines show the corresponding 16th and 84th percentiles. For calculating these curves, in the top panel, we ignore haloes which do not contain a central galaxy and in the bottom panel, we further ignore haloes whose central does not contain any H I mass. The solid purple curve in the top panel shows the SHAM calibration from Behroozi et al. (2013b), while the dash-dotted purple curve shows the same relation with parameters taken from Kravtsov et al. (2018), converted to the m_{200b} mass definition in each case. The horizontal dotted lines in each panel indicate the approximate completeness thresholds for m_* and m_{HI} in the mock.

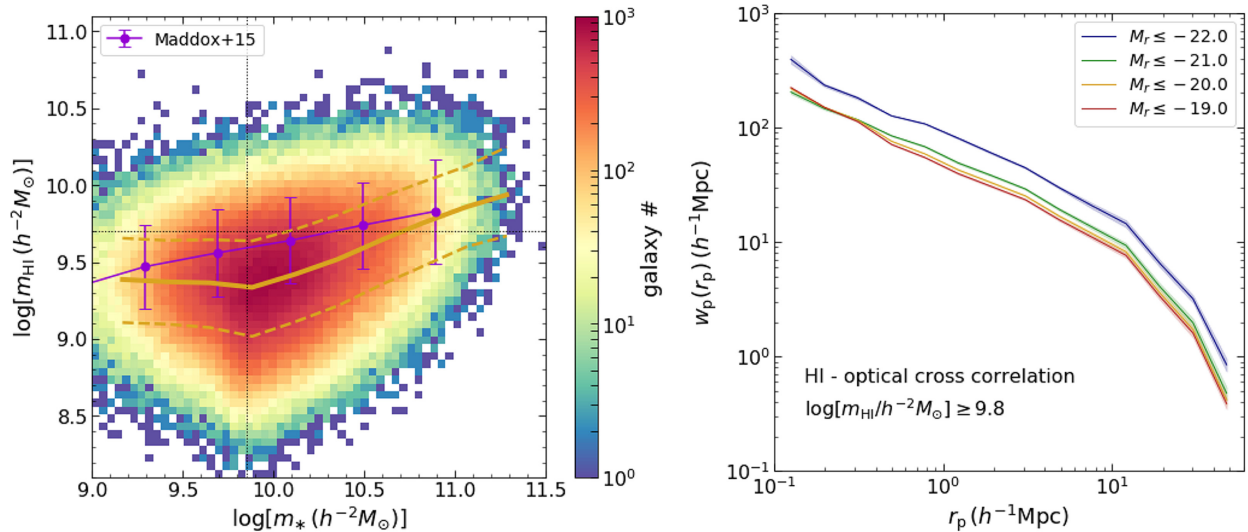


Figure 13. Predictions of optical-HI correlations not used in constraining the galaxy-dark matter connection in our mocks. (*Left-hand panel*): Joint distribution (coloured histogram) of m_{HI} and m_{*} for galaxies containing HI in one mock using the L300_N1024 box. Solid yellow line indicates the median m_{HI} in bins of m_{*} , while dashed yellow lines indicate the 16th and 84th percentiles. Vertical and horizontal dotted lines indicate the completeness limits of the mock in m_{*} and m_{HI} , respectively (see Figs 8 and 10). For comparison, the purple symbols with error bars show the relation calibrated by Maddox et al. (2015, see their table 1) using a cross-matched sample of HI-selected galaxies from the ALFALFA and SDSS surveys. (*Right-hand panel*): 2-point projected cross-correlation function between galaxy samples selected by optical luminosity thresholds (indicated by colours) and a sample selected by HI mass threshold (indicated in the label) using 3 realizations of the L300_N1024 configuration. The samples lie in the same volume and therefore overlap in membership, but are not explicitly cross-matched during their selection.

Fig. 13 shows the $m_{\text{HI}}-m_{*}$ relation (*left-hand panel*) and the spatial cross-correlation function between galaxy samples selected by luminosity and HI mass (*right-hand panel*) in our mocks. These are genuine predictions of our algorithm; comparing these with corresponding measurements forms a test of the various underlying assumptions. Indeed, as already noted by PCP18, we see in the left-hand panel that the predicted $m_{\text{HI}}-m_{*}$ relation is in reasonable agreement with the results of Maddox et al. (2015, purple points with errors), although the median trend in the mocks is slightly lower than in the data. Note, however, that our mocks are only complete above the m_{*} and m_{HI} thresholds indicated by the vertical and horizontal dotted lines, respectively. As such, a robust comparison with observations is not possible in the mass range we can explore.

To date, the only measurements of cross-correlations similar to those in the *right-hand panel* are by Papastergis et al. (2013), who studied the projected cross-2pcf between HI-selected galaxies in ALFALFA and colour-selected galaxies in SDSS (see their figs 17 and 18). As pointed out by Guo et al. (2017); however, the weights used by Papastergis et al. (2013) in their 2pcf measurements did not accurately account for sample variance effects, which are substantial in the small volume ($z \lesssim 0.05$) probed by the ALFALFA survey. For example, Guo et al. (2017) reported a significant m_{HI} -dependence of clustering, which was not detected by Papastergis et al. (2013).

It will therefore be very interesting to confront our mock catalogues with more robust cross-2pcf measurements. For example, the choices controlling HI-satellites in our model (namely, the value of the threshold halo mass $m_{\text{sat,max}}$) affect the shape of the cross-correlation at small separations between bright optical galaxies and HI-selected galaxies and can therefore be tested by such observations.

5.3 Possible extensions

Although the mocks we have presented here provide fairly realistic descriptions of the distribution of optical and HI properties of local

Universe galaxies, they contain several ingredients which can be potentially improved upon or extended. We list some of these here.

5.3.1 Assembly bias

We noted in Section 3.1 that our assignment of halo concentrations c_{200b} preserves spatial correlations of c_{200b} at fixed halo mass (also called assembly bias) under the assumption that these correlations are accurately tracked even by poorly resolved haloes. Recently, Ramakrishnan et al. (2020) have shown that this assumption fails at worse than ~ 20 per cent for haloes resolved with $\lesssim 150$ particles. Instead, they showed that the spatial correlations of the local tidal anisotropy α are accurately preserved even for haloes with as few as 30 particles. Using their technique of sampling a conditional distribution $p(c_{200b}|m, \alpha)$, therefore, will be a promising extension of our algorithm that would endow mocks built on low-resolution N -body simulations with accurate representations of halo assembly bias. Another interesting extension, also easy to include in our mocks, would be an environment-dependent modulation of the HOD itself, as discussed by Xu et al. (2020). Combined with the conditional sampling of halo properties, this would lead to full flexibility in modelling galaxy assembly bias.

5.3.2 Stellar disc-bulge decomposition

We also noted above that our treatment of the stellar spatial profile is, strictly speaking, inconsistent because it assumes a spherically symmetric distribution of stars rather than, say, an axially symmetric disc. Since our primary intention is to produce a rotation curve for each galaxy, the difference between a spherical bulge and an axial disc can potentially be a large effect (Binney & Tremaine 1987). We intend to explore this further in a forthcoming work, by simultaneously modelling a stellar disc and bulge using realistic bulge-to-disc mass

ratios (e.g. Bernardi et al. 2014), along with their correlations with galaxy colours and the presence of an H I disc.

5.3.3 Gas fractions

In this work, we used the expression (9) for the bound gas fraction f_{bgas} , with parameters adopted from ST15, for modelling all central galaxies with $M_r \leq -19$. Strictly speaking, this relation holds for the central galaxies of haloes with $m_{\text{vir}} \gtrsim 10^{13} h^{-1} M_{\odot}$, since it is calibrated using X-ray observations of galaxy clusters. Our choice therefore corresponds to an extrapolation of this relation into an unobserved regime of halo mass. Since the resulting value of f_{bgas} for each central is typically substantially smaller than its f_{egas} (which is set by baryonic mass conservation in this work), we do not expect this extrapolation to lead to any significant systematic error for any of the statistics explored in this paper. Improvements to this model could potentially explore using observations of the circumgalactic medium to first constrain f_{egas} .

5.3.4 Predictions at higher redshift

All of our results have been restricted to the local Universe, a consequence of using clustering constraints from the low-redshift ($z \lesssim 0.1$) surveys *SDSS* and *ALFALFA*. It will be interesting to extend our results to the redshift range $0.5 \lesssim z \lesssim 1$, which is interesting for both astrophysics and cosmology, and is the target of several completed, ongoing and upcoming galaxy surveys. In future work, we will explore whether an extension of our low-redshift algorithm, augmented by simplified galaxy evolution models (e.g. Lilly et al. 2013), can be used to make robust predictions at these higher redshifts.

6 CONCLUSION

The ability to realistically reproduce, in a simulated universe, the properties and spatial distribution of galaxies observed in the actual Universe, opens the door to addressing a number of interesting astrophysical and cosmological questions. We have presented an updated algorithm that produces catalogues of mock galaxies in simulated haloes at $z \approx 0$, realistically endowed with a variety of properties including r -band luminosities, $g - r$ and $u - r$ colours, stellar masses m_* , neutral hydrogen (H I) masses $m_{\text{H I}}$, as well as (for central galaxies) the spatial distribution of gas and stars, leading to realistic rotation curves. Our mock galaxies additionally inherit a number of environmental properties from their host dark matter haloes, including the halocentric overdensity, tidal anisotropy, and large-scale halo bias.

Our algorithm, which relies on an HOD that assigns galaxy properties based on halo mass m alone, can optionally include effects such as galactic conformity and colour-dependent galaxy assembly bias, and is easily extendable to include effects such as environment-dependent modulations of the HOD. By construction, the basic mocks we presented here reproduce the luminosity function, colour–luminosity relation and the luminosity- and colour-dependent 2-point clustering of optically selected *SDSS* galaxies with $M_r \leq -19$, as well as the H I mass function and H I-dependent 2-point clustering of H I-selected *ALFALFA* galaxies with $m_{\text{H I}} \gtrsim 10^{9.7} h^{-2} M_{\odot}$. The mocks then reproduce the *SDSS* stellar mass function and the *SDSS*–*ALFALFA* m_* – $m_{\text{H I}}$ relation reasonably well (these were not used when constraining the parameters of the algorithm), while predicting the spatial 2-point cross-correlation function of low-redshift optical

and H I galaxies (which has not yet been robustly measured; Fig. 13), and the m_* – m and $m_{\text{H I}}$ – m relations (Fig. 12). The calibrations we used lead to volume-completeness thresholds of $M_r \leq -19$, $m_* \gtrsim 10^{9.85} h^{-2} M_{\odot}$ and $m_{\text{H I}} \gtrsim 10^{9.7} h^{-2} M_{\odot}$, thus representing the population of massive galaxies in the low-redshift Universe. Our algorithm represents a consolidation of the results of Paranjape et al. (2015) and Paul et al. (2018, 2019).

Our mocks are potentially useful for a number of applications, some of which we list here.

(i) In their study of environment-dependent clustering in *SDSS*, Paranjape et al. (2018b) noted some small (~ 20 per cent) but significant differences between their ‘mass-only HOD’ mocks and *SDSS* galaxies in the most anisotropic tidal environments. These differences were ultimately inconclusive due to the comparable level of systematic uncertainties associated with the HOD calibration used by Paranjape et al. (2018b). The mocks we have presented, which are based on updated calibrations, largely mitigate many of these uncertainties. It will therefore be interesting to revisit this analysis to assess the level of beyond-mass effects induced by the tidal environment in the *SDSS* field (see also Alam et al. 2019).

(ii) As we noted earlier, our algorithm successfully describes H I-dependent clustering at the massive end in *ALFALFA* without the need of assembly bias, unlike earlier studies (e.g. Guo et al. 2017). Our mocks can therefore serve as useful null tests for galaxy assembly bias using interesting new combinations of observables, such as the large-scale bias of galaxies split by H I mass in bins of stellar mass.

(iii) Galactic conformity, a putative non-local connection between the satellites and central galaxy of the same halo, continues to pose a puzzle for galaxy formation models (Weinmann et al. 2006; Hearin, Behroozi & van den Bosch 2016b). Our mocks can be used to explore new tests of this phenomenon, e.g. the potential dependence of galactic conformity on tidal environment (which is otherwise an excellent indicator of halo assembly bias, see Ramakrishnan et al. 2019).

(iv) Our mocks can predict the H I mass function of (massive) galaxies selected by optical luminosity or colour. The corresponding measurements have only recently become available (Dutta, Khandai & Dey 2020; Dutta & Khandai 2021), and will be very useful for testing our basic assumptions regarding the connection between optical properties and H I.

(v) The rotation curves of our mock central galaxies, along with their H I discs when present, can be used to model the observed 21-cm velocity profiles of H I-selected galaxies. The distribution of the widths of these profiles has been measured in the *ALFALFA* survey (Papastergis et al. 2011; Moorman et al. 2014) and constitutes an exciting and hitherto unexplored new probe of the small-scale distribution of baryonic matter.

(vi) The ‘radial acceleration relation’ (RAR) between the acceleration profiles due to dark matter and baryons in disc galaxies (McGaugh, Lelli & Schombert 2016; Lelli et al. 2017) has emerged as an intriguing new probe of gravitational theories at galactic length-scales. The rotation curves and mass profiles of baryonic and dark matter in our mock central galaxies enable an exploration of the nature of the RAR for large samples of galaxies in the CDM+baryons framework (Paranjape & Sheth 2021).

ACKNOWLEDGEMENTS

We thank R. Srianand for his collaboration and for many valuable discussions and suggestions which improved the presentation of this paper. AP also thanks Nishikanta Khandai and Kandaswamy

Subramanian for insightful discussions. The research of AP is supported by the Associateship Scheme of ICTP, Trieste and the Ramanujan Fellowship awarded by the Department of Science and Technology, Government of India. TRC acknowledges support of the Department of Atomic Energy, Government of India, under project no. 12-R&D-TFR-5.02-0700 and the Associateship Scheme of ICTP. This work made extensive use of the open source computing packages NUMPY (Van Der Walt, Colbert & Varoquaux 2011),¹⁴ SCIPY (Virtanen et al. 2020),¹⁵ MATPLOTLIB (Hunter 2007),¹⁶ JUPYTER NOTEBOOK¹⁷, and the plotting software VEUSZ.¹⁸ We gratefully acknowledge the use of high performance computing facilities at IUCAA, Pune.¹⁹

DATA AVAILABILITY

The mock catalogues generated by our algorithm will be shared upon reasonable request to the authors.

REFERENCES

- Abadi M. G., Navarro J. F., Fardal M., Babul A., Steinmetz M., 2010, *MNRAS*, 407, 435
- Abazajian K. N. et al., 2009, *ApJS*, 182, 543
- Abbas U., Sheth R. K., 2007, *MNRAS*, 378, 641
- Alam S., Zu Y., Peacock J. A., Mandelbaum R., 2019, *MNRAS*, 483, 4501
- Alam S. et al., 2020, preprint([arXiv:2007.09004](https://arxiv.org/abs/2007.09004))
- Aricò G., Angulo R. E., Hernández-Montegudo C., Contreras S., Zennaro M., 2020a, preprint([arXiv:2009.14225](https://arxiv.org/abs/2009.14225))
- Aricò G., Angulo R. E., Hernández-Montegudo C., Contreras S., Zennaro M., Pellejero-Ibañez M., Rosas-Guevara Y., 2020b, *MNRAS*, 495, 4800
- Bagla J. S., Khandai N., Datta K. K., 2010, *MNRAS*, 407, 567
- Barnes J., White S. D. M., 1984, *MNRAS*, 211, 753
- Behroozi P. S., Wechsler R. H., Wu H.-Y., 2013a, *ApJ*, 762, 109
- Behroozi P. S., Wechsler R. H., Conroy C., 2013b, *ApJ*, 770, 57
- Behroozi P., Wechsler R. H., Hearin A. P., Conroy C., 2019, *MNRAS*, 488, 3143
- Bernardi M., Meert A., Vikram V., Huertas-Company M., Mei S., Shankar F., Sheth R. K., 2014, *MNRAS*, 443, 874
- Bett P., Eke V., Frenk C. S., Jenkins A., Helly J., Navarro J., 2007, *MNRAS*, 376, 215
- Binney J., Tremaine S., 1987, *Galactic Dynamics*. Princeton Univ. Press, Princeton, NJ
- Blanton M. R., Roweis S., 2007, *AJ*, 133, 734
- Blanton M. R. et al., 2003, *ApJ*, 592, 819
- Blumenthal G. R., Faber S. M., Flores R., Primack J. R., 1986, *ApJ*, 301, 27
- Castorina E., Villaescusa-Navarro F., 2017, *MNRAS*, 471, 1788
- Chisari N. E. et al., 2018, *MNRAS*, 480, 3962
- Contreras S., Angulo R., Zennaro M., 2020, preprint([arXiv:2012.06596](https://arxiv.org/abs/2012.06596))
- Cooray A., Sheth R., 2002, *Phys. Rep.*, 372, 1
- de la Torre S., Peacock J. A., 2013, *MNRAS*, 435, 743
- de la Torre S. et al., 2013, *A&A*, 557, A54
- Dempster A. P., Laird N. M., Rubin D. B., 1977, *J. R. Stat. Soc. Ser. B*, 39, 1
- Diemer B., Kravtsov A. V., 2015, *ApJ*, 799, 108
- Dubois Y. et al., 2014, *MNRAS*, 444, 1453
- Dutta S., Khandai N., 2021, *MNRAS*, 500, L37
- Dutta S., Khandai N., Dey B., 2020, *MNRAS*, 494, 2664
- Giovanelli R. et al., 2005, *AJ*, 130, 2598
- Gnedin O. Y., Kravtsov A. V., Klypin A. A., Nagai D., 2004, *ApJ*, 616, 16
- Guha Sarkar T., Mitra S., Majumdar S., Choudhury T. R., 2012, *MNRAS*, 421, 3570
- Guo H. et al., 2015, *MNRAS*, 453, 4368
- Guo H., Li C., Zheng Z., Mo H. J., Jing Y. P., Zu Y., Lim S. H., Xu H., 2017, *ApJ*, 846, 61
- Hahn O., Abel T., 2011, *MNRAS*, 415, 2101
- Hearin A. P., Watson D. F., 2013, *MNRAS*, 435, 1313
- Hearin A. P., Zentner A. R., van den Bosch F. C., Campbell D., Tollerud E., 2016a, *MNRAS*, 460, 2552
- Hearin A. P., Behroozi P. S., van den Bosch F. C., 2016b, *MNRAS*, 461, 2135
- Hu W., Kravtsov A. V., 2003, *ApJ*, 584, 702
- Hunter J. D., 2007, *Comput. Sci. Eng.*, 9, 90
- Kitaura F.-S. et al., 2016, *MNRAS*, 456, 4156
- Komatsu E. et al., 2011, *ApJS*, 192, 18
- Kravtsov A. V., 2013, *ApJ*, 764, L31
- Kravtsov A. V., Vikhlinin A. A., Meshcheryakov A. V., 2018, *Astron. Lett.*, 44, 8
- Lelli F., McGaugh S. S., Schombert J. M., Pawlowski M. S., 2017, *ApJ*, 836, 152
- Lewis A., Challinor A., Lasenby A., 2000, *ApJ*, 538, 473
- Lilly S. J., Carollo C. M., Pipino A., Renzini A., Peng Y., 2013, *ApJ*, 772, 119
- Maddox N., Hess K. M., Obreschkow D., Jarvis M. J., Blyth S. L., 2015, *MNRAS*, 447, 1610
- Manera M. et al., 2013, *MNRAS*, 428, 1036
- Mao Y.-Y. et al., 2018, *ApJS*, 234, 36
- Martin A. M., Papastergis E., Giovanelli R., Haynes M. P., Springob C. M., Stierwalt S., 2010, *ApJ*, 723, 1359
- Masaki S., Lin Y.-T., Yoshida N., 2013, *MNRAS*, 436, 2286
- McGaugh S. S., Rubin V. C., de Blok W. J. G., 2001, *AJ*, 122, 2381
- McGaugh S. S., Lelli F., Schombert J. M., 2016, *Phys. Rev. Lett.*, 117, 201101
- Meert A., Vikram V., Bernardi M., 2015, *MNRAS*, 446, 3943
- Mo H. J., Mao S., White S. D. M., 1998, *MNRAS*, 295, 319
- Moorman C. M., Vogeley M. S., Hoyle F., Pan D. C., Haynes M. P., Giovanelli R., 2014, *MNRAS*, 444, 3559
- Navarro J. F., Frenk C. S., White S. D. M., 1996, *ApJ*, 462, 563
- Obreschkow D., Croton D., De Lucia G., Khochfar S., Rawlings S., 2009, *ApJ*, 698, 1467
- Padmanabhan H., Refregier A., Amara A., 2017, *MNRAS*, 469, 2323
- Papastergis E., Martin A. M., Giovanelli R., Haynes M. P., 2011, *ApJ*, 739, 38
- Papastergis E., Giovanelli R., Haynes M. P., Rodríguez-Puebla A., Jones M. G., 2013, *ApJ*, 776, 43
- Paranjape A., Alam S., 2020, *MNRAS*, 495, 3233
- Paranjape A., Sheth R. K., 2021, preprint([arXiv:2102.13116](https://arxiv.org/abs/2102.13116))
- Paranjape A., Kovač K., Hartley W. G., Pahwa I., 2015, *MNRAS*, 454, 3030
- Paranjape A., Hahn O., Sheth R. K., 2018a, *MNRAS*, 476, 3631
- Paranjape A., Hahn O., Sheth R. K., 2018b, *MNRAS*, 476, 5442
- Paul N., Choudhury T. R., Paranjape A., 2018, *MNRAS*, 479, 1627
- Paul N., Pahwa I., Paranjape A., 2019, *MNRAS*, 488, 1220
- Pedregosa F. et al., 2011, *J. Mach. Learn. Res.*, 12, 2825
- Peng Y.-J., Lilly S. J., Renzini A., Carollo M., 2012, *ApJ*, 757, 4
- Persic M., Salucci P., Stel F., 1996, *MNRAS*, 281, 27
- Ramakrishnan S., Paranjape A., Hahn O., Sheth R. K., 2019, *MNRAS*, 489, 2977
- Ramakrishnan S., Paranjape A., Sheth R. K., 2020, preprint([arXiv:2012.10170](https://arxiv.org/abs/2012.10170))
- Reddick R. M., Wechsler R. H., Tinker J. L., Behroozi P. S., 2013, *ApJ*, 771, 30
- Schaye J. et al., 2015, *MNRAS*, 446, 521
- Schneider A., Teyssier R., 2015, *J. Cosmol. Astropart. Phys.*, 2015, 049
- Schneider A., Teyssier R., Stadel J., Chisari N. E., Le Brun A. M. C., Amara A., Refregier A., 2019, *J. Cosmol. Astropart. Phys.*, 2019, 020
- Scoccimarro R., 1998, *MNRAS*, 299, 1097
- Skibba R. A., Sheth R. K., 2009, *MNRAS*, 392, 1080
- Somerville R. S., Davé R., 2015, *ARA&A*, 53, 51
- Springel V., 2005, *MNRAS*, 364, 1105
- Springel V. et al., 2018, *MNRAS*, 475, 676

¹⁴<http://www.numpy.org>

¹⁵<http://www.scipy.org>

¹⁶<https://matplotlib.org/>

¹⁷<https://jupyter.org>

¹⁸<https://veusz.github.io/>

¹⁹<http://hpc.iucaa.in>

- Sugiyama S., Takada M., Kobayashi Y., Miyatake H., Shirasaki M., Nishimichi T., Park Y., 2020, *Phys. Rev. D*, 102, 083520
- Teyssier R., Moore B., Martizzi D., Dubois Y., Mayer L., 2011, *MNRAS*, 414, 195
- Tinker J., Kravtsov A. V., Klypin A., Abazajian K., Warren M., Yepes G., Gottlöber S., Holz D. E., 2008, *ApJ*, 688, 709
- Vale A., Ostriker J. P., 2004, *MNRAS*, 353, 189
- van den Bosch F. C., Aquino D., Yang X., Mo H. J., Pasquali A., McIntosh D. H., Weinmann S. M., Kang X., 2008, *MNRAS*, 387, 79
- Van Der Walt S., Colbert S. C., Varoquaux G., 2011, preprint(arXiv:1102.1523)
- Villaescusa-Navarro F., Viel M., Datta K. K., Choudhury T. R., 2014, *J. Cosmol. Astropart. Phys.*, 2014, 050
- Virtanen P. et al., 2020, *Nat. Methods*, 17, 261
- Vogelsberger M. et al., 2014, *MNRAS*, 444, 1518
- Wang W., White S. D. M., 2012, *MNRAS*, 424, 2574
- Wang J., Koribalski B. S., Serra P., van der Hulst T., Roychowdhury S., Kamphuis P., Chengalur J. N., 2016, *MNRAS*, 460, 2143
- Weinmann S. M., van den Bosch F. C., Yang X., Mo H. J., 2006, *MNRAS*, 366, 2
- Xu H., Zheng Z., Guo H., Zu Y., Zehavi I., Weinberg D. H., 2018, *MNRAS*, 481, 5470
- Xu X., Zehavi I., Contreras S., 2020, *MNRAS*, 502, 3242
- Yang X., Mo H. J., van den Bosch F. C., Pasquali A., Li C., Barden M., 2007, *ApJ*, 671, 153
- Yang X. et al., 2018, *ApJ*, 860, 30
- York D. G. et al., 2000, *AJ*, 120, 1579
- Yuan S., Eisenstein D. J., Garrison L. H., 2018, *MNRAS*, 478, 2019
- Zehavi I. et al., 2011, *ApJ*, 736, 59
- Zentner A. R., Hearin A. P., van den Bosch F. C., 2014, *MNRAS*, 443, 3044
- Zhao C. et al., 2020, *MNRAS*, 503, 1149
- Zheng Z., Guo H., 2016, *MNRAS*, 458, 4015
- Zu Y., Mandelbaum R., 2015, *MNRAS*, 454, 1161

APPENDIX A: QUASI-ADIABATIC RELAXATION

Here, we describe the technique for calculating the response of the dark matter profile to presence of baryonic matter through an approximate conservation of angular momentum (Barnes & White 1984; Blumenthal et al. 1986; Gnedin et al. 2004; Abadi et al. 2010; Teyssier et al. 2011; ST15). The discussion below follows section 2.3 of ST15 (see their equations 2.15–2.17).

The basic equation describing this quasi-adiabatic relaxation gives the final radius r of a spherical dark matter element in terms of its initial radius r_{in} ,

$$\frac{r}{r_{\text{in}}} = 1 + q_{\text{rdm}} \left(\frac{m_{\text{nfw}}(< r_{\text{in}})}{m_{\text{tot}}(< r)} - 1 \right). \quad (\text{A1})$$

Here, $m_{\text{tot}}(< r) = m_{\text{bary}}(< r) + m_{\text{rdm}}(< r)$ is the total mass contained inside the final radius r , with $m_{\text{bary}}(< r) = 4\pi \int_0^r dr' r'^2 f_{\text{bary}} \rho_{\text{bary}}(r')$ being the baryonic component and $m_{\text{rdm}}(< r)$ being the final, relaxed

dark matter mass profile which satisfies

$$m_{\text{rdm}}(< r) = f_{\text{rdm}} m_{\text{nfw}}(< r_{\text{in}}), \quad (\text{A2})$$

and $m_{\text{nfw}}(< r_{\text{in}}) = 4\pi \int_0^{r_{\text{in}}} dr' r'^2 \rho_{\text{nfw}}(r')$ is the dark matter mass inside the *initial* radius as per the original, normalized NFW profile. We remind the reader that all the density profiles are normalized so as to enclose the entire mass m_{vir} inside $r = R_{\text{vir}}$.

The quantity q_{rdm} is a parameter controlling the level of angular momentum conservation. From equation (A1), we see that $q_{\text{rdm}} = 1$ corresponds to perfect conservation, since $r m(< r)$ is an adiabatic invariant in this case. On the other hand, $q_{\text{rdm}} = 0$ corresponds to no baryonic backreaction. In this work, we follow ST15 and set $q_{\text{rdm}} = 0.68$, which has been found to accurately describe the cumulative effects of baryonic backreaction effects both in the inner and outer regions of simulated haloes, accounting for the fact that the formation of the central galaxy is not instantaneous. The effect of varying q_{rdm} on rotation curves and related statistics will be the focus of a future study.

Defining the ratio

$$\xi \equiv r/r_{\text{in}}. \quad (\text{A3})$$

Equation (A1) can be re-written as

$$\begin{aligned} \mathcal{L}(\xi|r) &\equiv \xi - 1 + q_{\text{rdm}} - \frac{q_{\text{rdm}}}{f_{\text{rdm}}} \left[1 + \frac{m_{\text{bary}}(< r)}{f_{\text{rdm}} m_{\text{nfw}}(< r/\xi)} \right]^{-1} \\ &= 0, \end{aligned} \quad (\text{A4})$$

which is conducive to an iterative solution. We employ Newton's method using an analytical expression for the derivative $\mathcal{L}'(\xi|r) = \partial \mathcal{L}(\xi|r) / \partial \xi$ at fixed r and writing the estimate at the n th iteration as

$$\xi^{(n)} = \xi^{(n-1)} - \frac{\mathcal{L}(\xi^{(n-1)}|r)}{\mathcal{L}'(\xi^{(n-1)}|r)}. \quad (\text{A5})$$

For practically all baryonic configurations and values of $r \in (10^{-3}, 1) \times R_{\text{vir}}$, and for all values $0 \leq q_{\text{rdm}} \leq 1$, convergence is achieved with a relative tolerance of 10^{-5} in $\lesssim 8$ iterations using equation (A5). (In contrast, a simple iteration applied directly to equation (A4) typically requires several tens to hundreds of iterations for $q_{\text{rdm}} \lesssim 0.8$, while the inner regions of the halo do not converge for $q_{\text{rdm}} \gtrsim 0.9$.)

Knowing the ratio ξ at any r then gives the mass of relaxed dark matter enclosed in radius r using equation (A2) setting $r_{\text{in}} = r/\xi$ on the right-hand side. By construction, $\xi = 1$ at $r = R_{\text{vir}}$, so that $m_{\text{rdm}}(< R_{\text{vir}}) = f_{\text{rdm}} m_{\text{vir}}$, as it should be. The value of $m_{\text{rdm}}(< r)$ at any r is sufficient for calculating the rotation curve $v_{\text{rot}}(r)$ using equation (11). For the differential profile shown in Fig. 4, we must differentiate equation (A2) with respect to r . The (somewhat cumbersome) result can be written analytically entirely in terms of ξ and r ; we omit it for brevity.

This paper has been typeset from a \LaTeX file prepared by the author.